



**HAL**  
open science

## Spatial variability of Quaternary denudation rates across a volcanic ocean island (Santo Antão, Cape Verde) from cosmogenic $^3\text{He}$

Camille Litty, Julien Charreau, Pierre-henri Blard, Raphaël Pik, Sébastien Nomade

### ► To cite this version:

Camille Litty, Julien Charreau, Pierre-henri Blard, Raphaël Pik, Sébastien Nomade. Spatial variability of Quaternary denudation rates across a volcanic ocean island (Santo Antão, Cape Verde) from cosmogenic  $^3\text{He}$ . *Geomorphology*, 2021, 375, pp.107557. 10.1016/j.geomorph.2020.107557. hal-03089201

**HAL Id: hal-03089201**

**<https://cnrs.hal.science/hal-03089201>**

Submitted on 28 Dec 2020

**HAL** is a multi-disciplinary open access archive for the deposit and dissemination of scientific research documents, whether they are published or not. The documents may come from teaching and research institutions in France or abroad, or from public or private research centers.

L'archive ouverte pluridisciplinaire **HAL**, est destinée au dépôt et à la diffusion de documents scientifiques de niveau recherche, publiés ou non, émanant des établissements d'enseignement et de recherche français ou étrangers, des laboratoires publics ou privés.

# 1 **Spatial variability of Quaternary denudation rates across a volcanic ocean** 2 **island (Santo Antão, Cape Verde) from cosmogenic $^3\text{He}$**

3 *Camille Litty<sup>1,2</sup>, Julien Charreau<sup>2</sup>, Pierre-Henri Blard<sup>2</sup>, Raphael Pik<sup>2</sup>, Sébastien Nomade<sup>3</sup>*

4 *<sup>1</sup>Université Grenoble Alpes, CNRS, IRD, IFSTTAR, ISTERRE, 38000 Grenoble, France*

5 *<sup>2</sup>Centre de Recherches Pétrologiques et Géochimiques, CRPG Nancy, France*

6 *<sup>3</sup>Université Versailles Saint-Quentin et Paris-Saclay, CEA Saclay, CNRS UMR 8212 Laboratoire des*  
7 *Sciences du Climat et de l'Environnement, Gif-sur-Yvette, France*

8 Corresponding authors : Dr. Camille Litty, [camille.litty@univ-grenoble-alpes.fr](mailto:camille.litty@univ-grenoble-alpes.fr)

9

## 10 **Abstract**

11 Denudation of volcanic ocean islands creates remarkable landscapes and contributes to Earth's  
12 carbon cycle, since the chemical alteration of basalts is a CO<sub>2</sub> sink. Because many volcanic islands have  
13 large climate gradients and relatively low variations in lithology and tectonic history, they represent  
14 excellent natural laboratories for studying climatic effects on landscape evolution. However, little is  
15 known about the control of denudation rates in ocean islands and the respective influences of climatic  
16 gradients and morphological parameters. Here, we present new measurements of long-term denudation  
17 rates from Santo Antão Island, Cape Verde (17°N). In this 779 km<sup>2</sup> island, mean annual precipitation  
18 ranges from 40 mm.yr<sup>-1</sup> in the southwest to 1100 mm.yr<sup>-1</sup> in the north. To constrain the spatial  
19 distribution of denudation rates, we measured the cosmogenic  $^3\text{He}$  concentration in river-transported  
20 pyroxene grains from 23 river bedload samples. We obtained basin wide denudation rates ranging from  
21  $2.7 \pm 0.1$  to  $57.5 \pm 0.3$  m/Ma. The denudation rates display a significant spatial variability, with the  
22 highest rates in catchments located in the northeast side of the island where modern precipitation are the  
23 highest and low denudation rates in the southern and western dry basins. Our study shows that  
24 precipitation is the main control on denudation and landscape development of the Santo Antão volcanic  
25 island. This study provides for the first time the spatial distribution of denudation rates across a volcanic  
26 island located in a tropical zone.

27

## 28 **1. Introduction**

29 Climate is thought to be one of the main parameters controlling denudation rates (e.g., Portenga  
30 and Bierman, 2011), which in turn impact many processes such as the building and evolution of  
31 mountain ranges (e.g., Willett, 1999; Whipple, 2009). Understanding the effects of climate on  
32 denudation rates is therefore thought to be critical, but the modality of its impact remain a matter of  
33 long-standing debate (e.g., Langbein and Schumm, 1958; DiBiase and Whipple, 2011). Conversely,  
34 denudation may also exert a strong feedback on climate at the geological time scale (e.g., Berner et al.,  
35 1983). Silicate weathering on continents consumes CO<sub>2</sub> and releases cations (Ca, Mg, K, Na) to the  
36 ocean. In the ocean, Ca and Mg are then combined with CO<sub>3</sub><sup>2-</sup> and precipitated into bicarbonate, resulting

37 in a net CO<sub>2</sub> sink (e.g., Berner et al, 1983). The weathering of basaltic lithologies are thus supposed to  
38 be an efficient CO<sub>2</sub> sink at the geological time scale (Dessert et al., 2003).

39 In such context, volcanic islands in tropical areas are noteworthy natural laboratories allowing  
40 the investigation of links and interactions between denudation and climatic processes for two main  
41 reasons. First, the amplitude of the denudation variations can be compared to climate only. Indeed, most  
42 of the volcanic islands often exhibit a strong climatic gradient, while tectonic and lithological forcing  
43 are comparatively negligible (Hildenbrand et al., 2008; Salvany et al., 2012; Jefferson et al., 2014).  
44 Second, according to geochemical measurements of dissolved load in rivers, the modern weathering of  
45 volcanic islands, especially in tropical areas, is especially intense (e.g., Louvat and Allègre, 1997,  
46 Jefferson et al., 2014). It may represent up to 35% of the total CO<sub>2</sub> consumed from continental silicate  
47 weathering (Gaillardet et al., 1999) and, hence, have a large influence on long-term climate changes  
48 (Lenton and Britton, 2006).

49 In this general context, it is of the utmost importance to better constrain denudation rates (i.e.,  
50 the sum of physical and chemical erosion) and their spatial distribution across these islands. Several  
51 studies have estimated the long-term (10<sup>5</sup>-10<sup>6</sup> a) denudation rates of several islands by reconstructing  
52 the original volcanic surfaces and then by calculating the volumes removed by erosion (Hildenbrand et  
53 al., 2008; Salvany et al., 2012; Menéndez et al., 2008; Ferrier et al., 2013; Ricci et al., 2015). This  
54 geomorphological approach relies on the postulate that the construction of the volcanoes precedes their  
55 destruction by erosion. However, these two processes can be indeed coeval, which can hamper an  
56 accurate estimate of the initial pre-erosion surface. Moreover, it is often hazardous to accurately estimate  
57 the age of the original surfaces of the volcanoes. The derived denudation rates are therefore tied to large  
58 uncertainties and must be rigorously considered as minimum values (Hildenbrand et al., 2008). Other  
59 studies have constrained modern denudation rates from direct geochemical measurements of dissolved  
60 load in rivers (Louvat and Allègre, 1997; Ferrier et al., 2013). However, these estimates remain only  
61 strictly valid over short time scales (10<sup>1</sup>-10<sup>2</sup>a). Therefore, the mechanisms by which volcanic islands  
62 erode at the Quaternary time scale (10<sup>2</sup>-10<sup>4</sup>) remain largely unknown despite being a critical parameter  
63 for a comparison with long-term climate change.

64 Basin wide denudation rates at the Quaternary time scale can be quantified by measuring the  
65 concentration of cosmogenic nuclides in river sediment. In-situ cosmogenic nuclides are produced by  
66 the flux of secondary cosmic particles in the top few meters of Earth's surface (e.g., Granger et al., 1996).  
67 However, denudation rate measurements from cosmogenic nuclides have been mainly based on quartz-  
68 rich lithologies through <sup>10</sup>Be analyses (e.g., Granger et al., 1996). On basaltic and andesitic islands,  
69 quartz is rare or inexistent, implying that <sup>10</sup>Be cannot usually be used (Blard et al., 2008). Cosmogenic  
70 <sup>3</sup>He measured in pyroxene and olivine in river bedload sediment represents a good alternative to <sup>10</sup>Be  
71 for these mafic terrains (e.g., Puchol et al., 2017). These minerals have a high helium retentivity (Blard  
72 and Pik, 2008) and their <sup>3</sup>He cosmogenic production rate is relatively well established (Balco et al.,  
73 2008). <sup>3</sup>He has been widely used for the past 30 years to date lava flows (e.g., Kurz, 1986) or to

74 reconstruct continental paleoclimates (e.g., Blard et al., 2007). However, only a few studies have used  
75 cosmogenic  $^3\text{He}$  to estimate denudation rates (Gayer et al., 2008, Ferrier et al., 2013, Puchol et al., 2017).  
76 Sarda et al. (1993) were the first to determine denudation rates from cosmogenic  $^3\text{He}$  in a volcanic island,  
77 but this study was limited to a depth profile at one single location in La Reunion. To quantify Quaternary  
78 denudation rates Gayer et al. (2008) and Ferrier et al. (2013) measured the cosmogenic  $^3\text{He}$  in river sand  
79 in Kauaʻi Island (Hawaii), but both studies were limited to a single drainage basin.

80 In this paper, we analyze the  $^3\text{He}$  cosmogenic concentrations in pyroxenes and olivines of 23  
81 sand samples collected in 19 different modern riverbeds across the entire Santo Antão Island (Cape  
82 Verde). We hence determine, for the first time across a volcanic island, the near-whole spatial variability  
83 of denudation rates averaged over the last  $10^3$  to  $10^5$  ka.

84

## 85 **2. Geological and climatic settings of the Cape Verde islands and Santo Antão**

86 The Cape Verde archipelago ( $4033 \text{ km}^2$ ) includes 10 major and several smaller islands located  
87  $\sim 600$  km west of the African continent (Fig. 1). The development of the islands likely initiated 19 Ma  
88 ago with tholeiitic sills that intruded the Jurassic–Cretaceous sea-floor basement (Hayes & Rabinowitz,  
89 1975; Duncan & Jackson, 1977). Since 19 Ma, the volcanic activity has not migrated and has been well  
90 distributed across the islands until present (Mitchell et al., 1983; Plesner et al., 2002). The active  
91 volcanic activity is now limited to Fogo Island with the last eruption in 1995.

92 The climate of the Cape Verde archipelago is driven by the respective position of the subtropical  
93 high pressure of the North Atlantic (Açores anticyclone) and the Intertropical Convergence Zone  
94 (Mannaerts and Gabriels, 2000). The wet season lasts from July to October when the ITCZ, usually  
95 centered around the equator, shifts toward  $10\text{--}20^\circ\text{N}$  and brings 80% of the annual precipitation, whereas  
96 during the rest of the year, precipitation is scarce (Mannaerts and Gabriels, 2000).

97 Santo Antão is the northernmost and second largest island ( $770 \text{ km}^2$ ) of the archipelago (Fig. 1).  
98 Its elevation ranges from 0 to 1979 m (Tope de Coroa), with a mean elevation of 362 m. The relief of  
99 the island forms a major orographic barrier that creates a large precipitation gradient with annual  
100 precipitation that varies by a factor of 20-30 between the wettest northeast and the driest southwest sides  
101 (Fig. 3a). Local rainfall is also strongly dependent on elevation, with some low coastal areas having low  
102 rainfall of  $0 - 150 \text{ mm.yr}^{-1}$  whereas the mountain areas above 1000 m elevation receive  $\sim 800 - 1000$   
103  $\text{mm.yr}^{-1}$  (Fig. 3a; Mannaerts and Gabriels, 2000). This precipitation gradient seems to have induced  
104 significant topographic heterogeneities across the island: major valleys on the north and northeast side  
105 of the island receive regular rain during the wet season and are deeply incised. In contrast, the southern  
106 part of the island receives only very irregular rain and the topography exhibits wide smooth seaward  
107 slopes preserving volcanic surfaces that are poorly incised (Fig. 3b). In addition, two deep ( $>1$  km) and  
108 large ( $> 5\text{km}$ ) circular depressions are located in Tarrafal and the Cha di Morte regions (Fig. 2 and 3).  
109 These two depressions together with the deeply entrenched valley in the north provide numerous

110 outcrops of the lavas that built the island and enable a good reconstruction of its volcanic history (e.g.,  
111 Plesner et al., 2002; Holm et al., 2005).

112 On Santo Antão, the oldest lavas reported are ~7.5 Ma old altered picrites and ankaramites of  
113 the Dos Bodes formation. They can be observed in a limited area at the bottom of the Cha di Morte  
114 depression (Plesner et al., 2002; Holm et al., 2005; Fig. 2). This formation is overlain by the thick (~800  
115 m) 3-1 Ma old Cha di Morte formation (Fig. 2; Plesner et al., 2002). The lava flows of this formation  
116 dip toward the coast and point toward sources of magma emission located in the central part of the  
117 island. The Dos Bodes and Cha di Morte formations are usually mapped together as “Older Volcanics”  
118 by several authors (Fig. 2; Holm et al., 2005). After the emplacement of the Cha di Morte formation,  
119 between ~1.4 Ma and 0.3 Ma, other lavas flows were emplaced in other areas of the island, indicating  
120 that the recent volcanic activity was less focused and more distributed (Plesner et al., 2002, Holm et al.  
121 2005). The Tope de Coroa volcano experienced a large flank collapse that is not yet dated and yields to  
122 the large Tarrafal circular depression. This depression was later refilled by the development of the  
123 modern Tope de Coroa stratovolcano ~0.1 Ma ago. Since ~0.3 Ma, the volcanic activity of the island is  
124 mainly characterized by explosive magmatism including numerous individual scoria cones,  
125 phreatomagmatic to strombolian and several pluri-meter-thick phonolitic to tephri-phonolitic tephra  
126 deposits referenced as the Cao Grande formation (Plesner et al., 2002; Eisele et al., 2015). During this  
127 recent explosive period, several lava flows are reported in the Tope de Coroa and in the Porto Novo  
128 region.

129

130

### 131 3. Material and methods

#### 132 3.1 Basin average denudation rates

133 Assuming isotopic steady state, meaning that the cosmogenic production of  $^3\text{He}$  is balanced by  
134 the erosional loss (Lal, 1991), approximating (similarly to the spallogenic production) the two muogenic  
135 production rates at depth with two different exponential laws, then the basin average denudation rate  
136 ( $\text{cm.yr}^{-1}$ ) is given by:

$$137 \bar{\epsilon} = \sum_{x=sp, \mu_{sm}, \mu_{fm}} \frac{\overline{P_{x,3}} \Lambda_x}{\rho_{3\text{He}_c}} \quad (1)$$

138

139 where the subscripts  $sp$ ,  $\mu_{sm}$  and  $\mu_{fm}$  correspond to the production by spallation, slow muon capture  
140 and fast muon processes, respectively.  $\overline{P_{x,3}}$  is the basin average *in situ* cosmogenic production rates at  
141 the surface ( $\text{at.g}^{-1}.\text{a}^{-1}$ ).  $\rho$  and  $\Lambda_x$  are the rock density ( $\text{g.cm}^{-3}$ ) and the attenuation length in the rocks ( $\text{g.cm}^{-2}$ )  
142 of each production pathway  $x$ , respectively.  $^3\text{He}_c$  ( $\text{at/g}$ ) is the mean concentration of the cosmogenic  
143  $^3\text{He}$  in the river sediment. We use a basalt density of  $3 \text{ g/cm}^3$  and assumed constant attenuation lengths  
144 of  $160 \text{ g/cm}^2$ ,  $4320 \text{ g/cm}^2$  and  $1500 \text{ g/cm}^2$  for spallation, fast muons capture and slow muons processes  
145 (e.g. Braucher et al., 2011). The basin average production rates were computed using a cell-by-cell

146 approach and the SIG tool Basinga (Charreau et al., 2019) with a 30 m digital elevation model of the  
147 Santo Antão Island. The production rates of each of the cells of the DEM were scaled using the time  
148 dependent Lal-Stone scheme (Stone, 2000), and a reference surface production at sea level and high  
149 latitude of  $122 \pm 12 \text{ at.g}^{-1}.\text{a}^{-1}$  has been used (world-wide mean of all calibration studies computed with  
150 the CREp calculator, Martin et al., 2017). Following DiBiase (2018), we did not apply any topographic  
151 shielding correction.

152

### 153 *3.2 Determination of cosmogenic $^3\text{He}$ in pyroxenes and olivines*

154 The total  $^3\text{He}$  concentration ( $^3\text{He}_{\text{tot}}$ ) in both pyroxenes and olivine is a three-component system  
155 (Blard and Farley, 2008) that can be written as follows:

$$156 \quad ^3\text{He}_{\text{tot}} = ^3\text{He}_c + ^3\text{He}_{\text{mag}} + ^3\text{He}_{\text{nucl}} \quad (2)$$

157 where indices *c*, *mag* and *nucl* refer to the concentration in matrix-sited cosmogenic  $^3\text{He}$ , the magmatic  
158  $^3\text{He}$  located in fluid and melt inclusions and the nucleogenic  $^3\text{He}$  produced by neutron capture on Li  
159 nuclei since the eruption of the lavas, respectively.

160 Similarly, the total  $^4\text{He}$  budget is a two-component system consisting of magmatic  $^4\text{He}$  inherited  
161 in fluid and melt inclusions and matrix-sited radiogenic  $^4\text{He}$  mainly produced by the decay of  $^{238}\text{U}$ ,  $^{235}\text{U}$   
162 and  $^{232}\text{Th}$  since the eruption:

$$163 \quad ^4\text{He}_{\text{tot}} = ^4\text{He}_{\text{rad}} + ^4\text{He}_{\text{mag}} \quad (3)$$

164 Therefore, the cosmogenic  $^3\text{He}_c$  can be estimated from Eq (2) if the magmatic, the nucleogenic  
165 and the total  $^3\text{He}$  can be estimated independently with accuracy and precision. The  $^3\text{He}_{\text{tot}}$  can be  
166 measured by melting the sample. The nucleogenic contribution  $^3\text{He}_{\text{nucl}}$  can be calculated using the mean  
167 neutron flux, the Li concentration and the eruption age of the minerals (Andrews, 1982). In practice, we  
168 used here the major and trace elements and the Li-concentrations of the phenocrysts measured at the  
169 SARM in Nancy to compute this nucleogenic component (Table A.1).

170 Because it can be quite variable from one aliquot to another (e.g.s Puchol et al., 2017), the  
171 magmatic  $^3\text{He}_{\text{mag}}$  component is difficult to estimate. Magmatic He can be preferentially released and  
172 analyzed by in vacuo mineral crushing (Kurz, 1986). The crushing must, however, be sufficiently long  
173 to release and purge most of the trapped magmatic He. On the other hand, this crushing should not be  
174 too intense nor too long to avoid releasing the matrix sited  $^3\text{He}_c$  and/or the  $^4\text{He}_{\text{rad}}$  (Blard et al., 2006,  
175 2008), nor contaminate the sample with atmospheric He (Protin et al., 2016).

176 In the present study, we crushed all the pyroxenes/olivines and analyzed the  $^3\text{He}$  and  $^4\text{He}$   
177 concentrations extracted during this extraction step (“crush” indice). We fused in a high vacuum furnace  
178 additional uncrushed pyroxene/olivine aliquots (above  $1400^\circ\text{C}$ , to ensure a complete He release), and  
179 measured the  $^3\text{He}$  and  $^4\text{He}$  concentrations release (“melt” indice). Then, we describe and apply two  
180 approaches to estimate the magmatic component and to calculate the  $^3\text{He}$  cosmogenic concentration.  
181 Estimation of  $^3\text{He}_{\text{nucl}}$  is the same in both approaches.

182 The first approach is derived from the initial method proposed by (Kurz, 1986), and includes  
 183 the latter improvements by Dunai et al. (2000) and Blard and Farley (2008), to account for the presence  
 184 of  ${}^4\text{He}_{\text{rad}}$ . In this method, the cosmogenic  ${}^3\text{He}$  concentration is calculated as follow:

$$185 \quad {}^3\text{He}_c = {}^3\text{He}_{\text{tot}} - {}^3\text{He}_{\text{mag}} - {}^3\text{He}_{\text{nucl}}$$

$$186 \quad {}^3\text{He}_c = {}^3\text{He}_{\text{tot}} - [{}^4\text{He}_{\text{mag}} \times ({}^3\text{He}_{\text{mag}} / {}^4\text{He}_{\text{mag}})] - {}^3\text{He}_{\text{nucl}}$$

187 from Eq (3):

$$188 \quad {}^3\text{He}_c = {}^3\text{He}_{\text{tot}} - [({}^4\text{He}_{\text{tot}} - {}^4\text{He}_{\text{rad}}) \times ({}^3\text{He}_{\text{mag}} / {}^4\text{He}_{\text{mag}})] - {}^3\text{He}_{\text{nucl}}$$

189 and then:

$$190 \quad {}^3\text{He}_c = {}^3\text{He}_{\text{melt}} - [({}^4\text{He}_{\text{melt}} - {}^4\text{He}_{\text{rad}}) \times ({}^3\text{He}/{}^4\text{He})_{\text{crush}}] - {}^3\text{He}_{\text{nucl}} \quad (4)$$

191 The  $({}^3\text{He}/{}^4\text{He})_{\text{crush}}$  is the isotopic ratio measured during the initial crushing of the pyroxenes and  
 192 olivines, which is considered as representative of the magmatic isotopic ratio.

193 Because pedogenesis and sediment transport induces break up of phenocrysts, we consider that the  
 194 pyroxenes and olivines sampled in the riverbed loads do not bear any implanted  ${}^4\text{He}_{\text{rad}}$  from the (U-Th)  
 195 richer lava (Blard and Farley, 2008). This is justified because the implanted component is only present  
 196 in the 20  $\mu\text{m}$  outer rim (e.g., Dunai et al., 2000). Consequently, we computed the  ${}^4\text{He}_{\text{rad}}$  with the U-Th-  
 197 Sm concentrations measured in the sole phenocrysts (Tables 1 and A.2). To estimate the mean ages of  
 198 the lava flow, we used the geological map of List et al. (2007), and weighted each eruption age with the  
 199 respective contributive size of each studied basin. Additionally, if the measured  ${}^4\text{He}$  concentration during  
 200 melting is lower than the calculated  ${}^4\text{He}_{\text{rad}}$ , then we assume that the  ${}^4\text{He}_{\text{mag}}$  is null in these aliquots and  
 201 we only apply a correction for  ${}^3\text{He}_{\text{nucl}}$ .

202 The second approach assumes that the in vacuo crushing step was efficient enough to release all  
 203 the magmatic  ${}^3\text{He}$  from the aliquots and that the measured concentrations in the crushed aliquots are  
 204 representative of those of the melted aliquot. In this case, Eq. (2) can be rewritten as follows:

$$205 \quad {}^3\text{He}_c = {}^3\text{He}_{\text{melt}} - {}^3\text{He}_{\text{crush}} - {}^3\text{He}_{\text{nucl}} \quad (5)$$

206 with the indices *melt* and *crush* referring to the  ${}^3\text{He}$  measured after melting and crushing experiments of  
 207 the sample. The calculated cosmogenic  ${}^3\text{He}$  concentrations from both approaches, Eqs. (4) and (5) are  
 208 then used to estimate the average denudation rates in the different sampled river catchments on Santo  
 209 Antão Island applying Eq. (1) (e.g., Granger et al., 1996).

210

### 211 *3.3 Sampling, treatment and analyses*

212 Twenty-three samples were collected at the mouth of the main rivers all around the island (Fig.  
 213 3, Table A.1). Approximately 3 kg of river bedload sediment was collected from each sampling site.  
 214 Bulk sands were sieved under flowing water into the 0.15–0.5 mm granulometric fraction. A hand  
 215 magnet was first used to remove a large fraction of the magnetic sediment. Then the pyroxene and  
 216 olivine grains were concentrated from the sand by two magnetic separations using a Frantz device.  
 217 Nearly pure pyroxene and olivine grains were then obtained by gravimetric separation in di-iodomethane  
 218 (density  $\sim 3.3 \text{ g cm}^{-3}$ ). After washing in diethyl ether and drying, the grains were cleaned in an ultrasonic

219 bath of deionized water, and then acetone, for 10 min each, to remove any impurities resulting from  
220 dust. After drying, all grains with attached lava fragments were removed and discarded by handpicking  
221 under a binocular microscope. We chose to work mainly on pyroxenes because they were more abundant  
222 in our samples and thus easier to separate. Nevertheless, when olivines were present in some samples,  
223 we also analyzed mixed olivine/pyroxene aliquots. To measure the total  $^3\text{He}$  and  $^4\text{He}$  concentrations,  
224 grain aliquots were wrapped in copper foils and fused at  $1350^\circ\text{C}$  for 15 min. High temperature  
225 extractions were performed with the full metal induction furnace designed at CRPG (Zimmermann et  
226 al., 2012). After extraction, the gas was purified using activated charcoal at  $-196^\circ\text{C}$  and with hot ( $400^\circ\text{C}$   
227 and  $600^\circ\text{C}$ ) and ambient temperature ( $21^\circ\text{C}$ ) titanium sponge getters. A complete description of the  
228 furnace and the purification line can be found in Zimmermann et al. (2012). Helium was analyzed on a  
229 GV HELIX Split Flight Tube dual collector mass spectrometer. The instrument sensitivity was  
230 determined using the HESJ standard (Matsuda et al., 2002) whose certified  $^3\text{He}/^4\text{He}$  ratio is  $20.63 \pm 0.10$   
231 Ra (Ra =  $1.384 \times 10^{-6}$  being the atmospheric  $^3\text{He}/^4\text{He}$  ratio). To measure the  $\text{He}_{\text{mag}}$  concentration, in-  
232 vacuo crushing extractions were performed on additional aliquots with a soft iron slug activated by  
233 external solenoids (5 min at 100 strokes/min). After a first measurement, to optimize the release of all  
234 the  $\text{He}_{\text{mag}}$ , second crushing extractions of the same aliquot were performed. In the first approach, the  
235 mean value of the two crushing experiments was used to calculate the  $(^3\text{He}/^4\text{He})_{\text{crush}}$  ratios (i.e., the  
236 magmatic  $^3\text{He}/^4\text{He}$  ratio). In the second approach, the sum of the two crushing experiments has been  
237 used to compute the  $^3\text{He}_c$  as this approach assumes that the crushing extracts the whole magmatic He.  
238 Finally, to test the reproducibility of the methods, nine samples have been replicated and analyzed after  
239 high temperature extraction. For these replicates, magmatic corrections were performed using the same  
240 He results from in-vacuo crushing extraction.

241

#### 242 **4. Results**

243 Information about samples and catchment metrics are given in supplementary Table A.1. Annual  
244 precipitation rates have been estimated from the TRMM model with 20% of uncertainties and gradient  
245 information have been extracted from a 30 m resolution DEM (Table A.1). Helium results of the  
246 pyroxenes/olivines crushing are presented in Table A.1. Major and trace element concentrations used to  
247 calculate the  $^4\text{He}_{\text{rad}}$  and  $^3\text{He}_{\text{nuc}}$  components are given in supplementary Table A.2. Results of high  
248 temperature extractions and calculated  $^3\text{He}_c$  concentration and denudation rates are presented in Table  
249 1.

250 Mean  $^4\text{He}$  and  $^3\text{He}$  blanks during heating extraction were  $(7.3 \pm 0.3) \times 10^{-15}$  mol and  $(1.24 \pm$   
251  $0.2) \times 10^{-19}$  mol, respectively. Repeated measures after sample heating extraction always yielded He  
252 concentrations in the blank range, indicating that the extraction was complete after the first heating step.  
253 Mean  $^4\text{He}$  and  $^3\text{He}$  sample values during heating extraction before blank correction were  $(1.10 \pm 0.03)$   
254  $\times 10^{-12}$  mol and  $(4.2 \pm 0.2) \times 10^{-18}$  mol, respectively, one to three orders of magnitude higher than the

255 measured blank concentrations. This implies that blanks do not represent a significant source of  
256 uncertainty. Mean  $^4\text{He}$  and  $^3\text{He}$  blanks measured from the crushing device (with the slug moving) were  
257  $(8.6 \pm 0.4) \times 10^{-15}$  mol and  $(1.4 \pm 0.1) \times 10^{-19}$  mol, respectively. Mean  $^4\text{He}$  and  $^3\text{He}$  sample values for  
258 the crushing experiments before blank correction were  $(5.8 \pm 1.5) \times 10^{-14}$  mol and  $(6.5 \pm 1.7) \times 10^{-19}$   
259 mol, respectively. Blanks therefore represent 10 to 20% of the crushing concentrations. The calculated  
260 concentrations have been then corrected with the mean blank values.

261 This corresponds to total  $^4\text{He}$  and  $^3\text{He}$  concentrations measured after heating experiments  
262 ranging between  $(13 \pm 1) \times 10^{10}$  and  $(27 \pm 1) \times 10^{11}$  at/g and between  $(22 \pm 3) \times 10^5$  and  $(29 \pm 1.3) \times 10^6$   
263 at/g, respectively (Table 1). The magmatic  $^4\text{He}$  and  $^3\text{He}$  concentrations measured after the first in-vacuo  
264 crushing extractions range between  $(6.3 \pm 0.1) \times 10^9$  and  $(2.6 \pm 0.2) \times 10^{11}$  at/g and between  $(1.9 \pm 0.1)$   
265  $\times 10^4$  and  $(8.8 \pm 0.4) \times 10^6$  at/g, respectively (Table A.1). Corresponding  $^3\text{He}/^4\text{He}$  ratios measured by  
266 crushing range between  $2 \pm 14$  Ra and  $15 \pm 10$  with a weighted mean of  $12.2 \pm 0.3$  Ra ( $\text{Ra} = 1.384 \times 10^{-6}$   
267 being the atmospheric  $^3\text{He}/^4\text{He}$  ratio). Second in-vacuo crushing extractions show similar results and,  
268 when summed with the first crushing, returned total magmatic values that range between  $(6.3 \pm 0.1) \times$   
269  $10^9$  and  $(5.8 \pm 0.2) \times 10^{11}$  at/g and between  $(1.9 \pm 0.1) \times 10^4$  and  $(1.1 \pm 0.06) \times 10^7$  at/g for  $^4\text{He}$  and  $^3\text{He}$ ,  
270 respectively. The isotopic ratios of the two crushing together range between  $2 \pm 14$  Ra and  $14.1 \pm 0.9$   
271 Ra, with a weighted mean of  $11.8 \pm 0.4$  Ra. However, some samples have not been measured for a second  
272 in-vacuo crushing extraction.

273 With the first approach, calculated cosmogenic  $^3\text{He}$  concentrations range between  $(2.1 \pm 1.4) \times$   
274  $10^6$  at/g and  $(2.0 \pm 0.17) \times 10^7$  at/g (Table 1). Eight aliquots show  $^3\text{He}_{\text{mag}} > ^3\text{He}_{\text{melt}}$  therefore yielding null  
275 cosmogenic  $^3\text{He}_c$  concentrations. The second approach leads to  $^3\text{He}_c$  concentrations ranging between  
276  $(2.0 \pm 0.3) \times 10^6$  and  $(2.3 \pm 0.1) \times 10^7$  at/g. Importantly, the two approaches yield  $^3\text{He}_c$  concentrations  
277 and denudation rates that are close to the 1:1 line for most of the samples (Fig. 4a and b), indicating that  
278 the choice of the correction procedure for the non-cosmogenic  $^3\text{He}$  components is not a significant  
279 source of uncertainty. Based on these cosmogenic  $^3\text{He}$  concentrations, we determined the denudation  
280 rates of 23 samples in 19 main catchments all across the Santo Antão Island. Considering the two  
281 approaches, and ignoring the few samples that yielded null-cosmogenic  $^3\text{He}$  concentrations, denudation  
282 rates show a variability across the island, from  $2.7 \pm 0.1$  m/Ma (CV18-01) to  $58 \pm 4$  m/Ma (CV18-20),  
283 with a mean denudation rate over the studied catchments of  $18.0 \pm 5.2$  m/Ma. Finally, the nine replicated  
284 measurements are compatible within analytical uncertainties (Fig. 5a, b,c). For denudation rates lower  
285 than 15m/Ma, the correlation between replicates is robust and is not dependent on the approach (Fig.  
286 5d;  $R^2 = 0.76$ , p-value = 0.002).

287

## 288 5. Discussion

289 *5.1 Reliability of the calculated cosmogenic  $^3\text{He}$  concentrations and derived denudation rates*

290 The reconstruction of the  $^3\text{He}_c$  concentrations relies on several assumptions and corrections that  
291 must be considered. First, the two approaches give similar results, which suggest that the concentration  
292 in cosmogenic  $^3\text{He}$  has been accurately quantified. However, when looking in detail, the  $^3\text{He}_c$   
293 concentrations obtained with the second approach are lower by  $\sim 10$  to  $20\%$  compared to those of the  
294 first approach, for most of the samples (Fig. 4a), leading to  $\sim 10$  to  $20\%$  higher denudation rates (Fig.  
295 4b). The first approach depends on the accuracy of the  $^4\text{He}$  radiogenic and the magmatic ( $^3\text{He}/^4\text{He}$ )  
296 estimates. The assumption that the implanted radiogenic  $^4\text{He}$  from the (U-Th) richer lava can be  
297 neglected is supported by the fact that, if it is considered, computed radiogenic  $^4\text{He}$  are larger than the  
298 total  $^4\text{He}$  measured in almost  $90\%$  of the analyzed aliquots. On the other hand, the lower  $^3\text{He}_c$   
299 concentrations obtained with the first approach could suggest an underestimate of the  $^4\text{He}_{\text{rad}}$ . This could  
300 result from an underestimate of the eruption age of the bedrock material. Rivers may actually erode  
301 more efficiently the older lithologies than the younger ones. Alternatively, older rocks are porphyritic  
302 and probably contain more pyroxenes than the younger ones. However, we carefully estimated the mean  
303 bedrock ages in each basin, propagating high uncertainties considering the age distributions within a  
304 given basin (from  $10$  to  $93\%$ , average =  $60\%$ ; Table A.1). For that reason, the first approach yields  
305 higher uncertainties (mean  $1\sigma$  error of  $20\%$ ) than the second one (mean  $1\sigma$  error of  $10\%$ ). Second, the  
306 lower cosmogenic  $^3\text{He}$  concentrations calculated with the first approach compared to the second may  
307 also suggest an overestimation of  $(^3\text{He}/^4\text{He})_{\text{mag}}$  ratio from the crushing experiments. Too intense  
308 crushing could have partially released the  $^3\text{He}_c$  trapped in the crystal lattice (Blard et al., 2006, 2008).  
309 Moreover, the good reproducibility between the nine replicates suggests that merging hundreds of grains  
310 in each aliquot seems sufficient to average the  $^3\text{He}_c$  concentration, despite possible spatial variability of  
311 the denudation in the watershed (Puchol et al., 2017). Samples yielding denudation rates above  $\sim 15$   
312 m/Ma display an increase of the inter-aliquot scatter, with up to  $57\%$  of differences between the  
313 replicates (Fig. 5c). This observation suggests that, in Santo Antão Island,  $\sim 15$  m/Ma seems to be a  
314 threshold value, above which denudation rates can only be measured with lower accuracy and precision.  
315 This threshold is directly controlled by the cosmogenic/magmatic ratio, as well as by the amount of  
316 radiogenic  $^4\text{He}$ . It may thus vary from one geological setting to another and it may represent a significant  
317 limitation, particularly in catchments where denudation rates are high ( $\gg 10$  m/Ma; Puchol et al., 2017).

318 Foeken et al. (2012) have calibrated the local  $^3\text{He}$  cosmogenic production rate in the nearby  
319 Fogo Island to  $75.6 \pm 7.0$  at.g $^{-1}$ .yr $^{-1}$  in olivine and  $70.1 \pm 2.9$  at.g $^{-1}$ .yr $^{-1}$  in pyroxene. These values are  
320 significantly lower than other  $^3\text{He}$  production rates found elsewhere in the world and the reference  
321 surface production at sea level and high latitude of  $122 \pm 12$  at.g $^{-1}$ .yr $^{-1}$  (Martin et al., 2017) that we use in  
322 our calculations. Foeken et al. (2012) explained this discrepancy by geomagnetic field strength spatial  
323 variability. Considering these local production rates would decrease all our Cape Verde denudation rate  
324 values but would not change their relative spatial variations.

325

326 In summary, we conclude that we accurately measured and estimated the different He  
327 components and that the two approaches provide reliable estimates of the cosmogenic  $^3\text{He}_c$   
328 concentration. Because the uncertainties associated to the second approach are lower than those of the  
329 first one, and because both approaches produce results that are identical within uncertainties, we restrain  
330 the following discussion to the denudation rates derived from the second approach.

331

### 332 *5.2 Denudation rates variability in Santo Antão*

333 The studied hydrological basins of Santo Antão are characterized by a broad range of basin-  
334 averaged denudation rates, ranging between  $\sim 3$  and  $\sim 60$  m/Ma and therefore varying by a factor of 20  
335 across the island (Fig. 6; Table 1). The basins in the south and west sides of the island display the lower  
336 calculated denudation rates ranging from  $\sim 3$  and  $\sim 20$  m/Ma. One sample (CV18-26) located in the south  
337 of the island but shows a relatively high denudation rate ( $26.1 \pm 5.4$  m/Ma and  $36.6 \pm 4.4$  m/Ma with  
338 the first and second approach respectively) and compared to the other southern basins seems to be an  
339 outlier that is not representative of this subregion. The northern basins are characterized by a gradient  
340 of the denudation rates from the southeast to the northwest. Finally, the region of the Cha di Morte  
341 displays the highest denudation rates of the island, with values reaching  $\sim 60$  m/Ma (Fig. 6). These  
342 denudation rates inferred from  $^3\text{He}_c$  are averaged over characteristic timescales ( $T_{\text{int}} = (\Lambda/\rho)/\varepsilon$ ). In Santo  
343 Antão, the integrated timescale of these denudation rates ranges from  $\sim 10$  ka for the fastest eroded basins  
344 in the north, to  $\sim 200$  ka for the southern basins, with a mean value of  $\sim 50$  ka for the island (Table 1).  
345 However, in the south side of the island, the calculated integration time is in some places higher than  
346 the age of the rocks. This suggests that the southern side could exhibit even lower denudation rates than  
347 the calculated rates. This variability of long-term denudation rates variability across Santo Antão seem  
348 to correlate with the modern precipitation pattern on the island. Basins located in the northeast and  
349 receiving relatively high precipitation are characterized by the highest denudation rates. Basins located  
350 in the south receiving the lowest annual precipitation rates of the island yield the lowest denudation rates  
351 (Fig. 3a and 6). This observation is consistent with the study of Ferrier et al. (2013): by reconstructing  
352 the eroded volume in 24 basins across Kaua’I in Hawaii, these authors found that long-term (Ma)  
353 denudation rates on the island are correlated with modern annual precipitation.

354 However, given the typical integration time of our cosmogenic  $^3\text{He}$ -derived denudation rates of 53 ka,  
355 spatial patterns in precipitation rates may have been different in the past, meaning that the denudation  
356 rates we have measured could result from superimposed successive climatic settings. In Santo Antão,  
357 the trade winds have been stable since at least the last glacial maximum, 20 ka (Rognon et al., 1996).  
358 Another study even suggests that trade winds have been present over the last 140 ka (Hooghiemstra,  
359 1989). Such timescales are similar to, or longer than, the integration time of the cosmogenic  $^3\text{He}$ -derived  
360 denudation rates. This created a stable mean gradient of precipitation that caused one side of the island  
361 to erode at higher rates than the other. Moreover, during this time span the volcanic activity that could

362 have reshaped and reconstructed the surface of the islands was relatively limited (Plesner et al., 2002).  
363 Therefore, climatic conditions can explain the spatial variations of the long-term denudation rates across  
364 the island.

365 On the other hand, the topographic patterns also strongly vary across the island and is also in  
366 apparent correlation with the variability of denudation rates. Steeply sloping valleys are located in the  
367 northeast side of the island, in the Tarrafal and Cha di Morte depressions where denudation rates are  
368 high ( $> 40$  m/Ma). The southern side of the island presents relatively low denudation rates, a relatively  
369 smooth morphology and low slope angles (Fig. 7). Gayer et al. (2008) also explained variations in  
370 cosmogenic  $^3\text{He}$  measured in 26 samples across the Waimea basin in Kaua'I (Hawaii) by a non-linear  
371 link between denudation rates and hillslope gradient. Yet the topography of the island could be inherited  
372 from its volcanic construction (Lahitte et al., 2012) independently from the precipitation pattern.  
373 To better explore and separate the correlation existing between denudation rates, precipitation rates and  
374 slopes, we performed a principal component analysis (PCA) using XLSTAT software (Jolliffe, 2002).  
375 The PCA for the mean annual precipitation, mean and maximum slopes in the catchments resulted in a  
376 distance biplot of the first two principal axes shown in Fig. 8. The first and second axis explained 74.6%  
377 and 18.6% of the variance, respectively. Samples were grouped in five clusters according to their  
378 denudation rates (Fig. 8). The striking feature of this PCA is that basins with low denudation rates ( $< 10$   
379 m/Ma) present both low mean precipitation and low mean and maximum slopes at the same time. Basins  
380 with denudation rates between 10 and 40 m/Ma display both relatively high mean precipitation and  
381 relatively high slopes in the catchments. The sample CV18-26, which seemed to be an outlier from a  
382 visual point of view, is also an outlier here as it does not belong to the right part of the graph (Fig. 8).  
383 Past studies have suggested strong coupling and feedbacks between climate, denudation and landscape  
384 evolution in active mountain ranges (e.g., Willet, 1999; Whipple, 2009). This study reinforces this idea  
385 and moreover suggests that these coupling and feedback processes also exist on volcanic islands, and  
386 that these forcing are not necessarily linear. In Santo Antão, the precipitation patterns over time control  
387 the potential for physical erosion and weathering (Jefferson et al., 2014). The spatial variability of  
388 denudation rates influences the differential evolution of the morphology over the island, initiating a  
389 probable positive feedback: high precipitation led to higher denudation rates on the northeast side of the  
390 island, allowing for the creation of deeply incised basins with high slope angles, high drainage density  
391 and fluvial valleys that penetrate inland to the central part of the island, amplifying the local denudation.  
392 In contrast, low precipitation leading to relatively low denudation rates on the south side of the island  
393 causes the formation of weakly dissected basins with low slopes, little tributary development and lack  
394 of deep valleys. Over the long term, the morphology of the island may thus have enhanced the  
395 denudation variability through positive feedbacks with the slopes where high slopes contributing to  
396 increase the potential for fluvial erosion. Therefore, topography on the island seems to be controlled by  
397 denudation rates rather than the contrary, at least at the initial stage of the island history. Moreover,  
398 climatic conditions seem to be the predominant process that has shaped the morphology of Santo Antão.

399 However, the highest denudation rates of the island ( $> 40$  m/Ma) are correlated with high precipitation  
400 rates, but are not necessarily associated with the highest slopes, suggesting that other parameters, such  
401 as geological properties, may also play a role.

402 Similarly, denudation rates estimated for CV18-19 and CV18-20, which are two of the highest values  
403 of the island, but located in the lee side of the island, can also result from other causes. (i) The valley  
404 bottom of the Cha di Morte is filled by alluvial conglomeratic deposits that are incised by modern  
405 streams. Sediments that have been sampled can possibly be recycled material from paleo conglomeratic  
406 deposits. They therefore record paleo-denudation rates that can differ from the modern ones.  
407 Additionally, these conglomerates are also probably characterized by a higher erodibility than pristine  
408 lava flow basalts. (ii) The Cha di Morte depression has been interpreted as being close to the source of  
409 the older volcanic magma and numerous dike and sills are intruding into the Dos Bodes and Cha di  
410 Morte formations (Holm et al. 2005). Dikes can significantly influence basin dissection by  
411 compartmentalizing the volcanic structure into individual blocks and increase water infiltration  
412 (Hildenbrand et al., 2005). Thus, in the Cha di Morte depression, the relative high denudation rates can  
413 also possibly be caused by an increase of the chemical alteration or be associated with physical erosion  
414 through mass-wasting of individual blocks.

415

### 416 *5.3 Denudation rates in other volcanic islands in the world*

417 In Cape Verde, our denudation rates results obtained for Santo Antão, are ranging between  $\sim 3$   
418 and  $60$  m/Ma and are comparable to those calculated on other volcanic islands characterized by different  
419 climatic patterns. In Kaua'i Island, Hawaii, Ferrier et al (2013) computed denudation rates based on  
420 eroded volume that range between  $3$  and  $112$  m/Ma. For the same island, Gayer et al (2008) proposed a  
421 denudation rate of  $56$  m/Ma from cosmogenic  $^3\text{He}$  measured in 26 samples across the Waimea basin. In  
422 Gran Canaria, Canary Islands, denudation rates based on eroded volume range between  $0.1$  and  $240$   
423 m/Ma (Menéndez et al., 2008). One extreme value reaches  $975$  m/Ma, however, it has been measured  
424 in a small basin of  $2.3$  km<sup>2</sup>. We decided to discard this value as well as 14 other denudation rates that  
425 have been computed in basins smaller than  $5$  km<sup>2</sup>. This avoids most of the outliers that seem to be related  
426 to local effects related to small eroded volumes in modest catchments. Finally, in Tahiti-Nui, in French  
427 Polynesia, Hildebrand et al. (2008) calculated denudation rates between  $72$  and  $2700$  m/Ma. Results  
428 from the different volcanic islands show significant differences in the range and absolute value of the  
429 observed denudation rates. Despite the different techniques used to infer denudation rates, previous  
430 studies and our study can be directly compared as all techniques measure both the mechanical and  
431 chemical erosion (Kirchner et al., 2006; Ferrier et al., 2013). Remarkably, we observe a logarithmic  
432 correlation between the Quaternary denudation rates and the mean annual precipitation rates when  
433 considering the data of the four islands ( $R^2 = 0.63$ ,  $p$ -value  $< 0.001$ ; Fig. 9). Although these different  
434 islands have variable volcanic morphologies and lithology, resulting from different geodynamic  
435 contexts, climatic conditions seem to be a predominant control on the denudation rates, and therefore,

436 on landscape evolution not only in Santo Antão but also in other volcanic islands in general. Our results  
437 demonstrate the strong coupling through which climate influences the variability of denudation and  
438 show how climate acts to shape the landscape of volcanic islands.

439

440

## 441 **6. Conclusion**

442 We accurately measured long-term (over 10 ka to 200 ka timescale) denudation rates from  
443 cosmogenic  $^3\text{He}$  in pyroxene from 23 river bedload samples in Santo Antão Island. The calculation of  
444 the long-term denudation rates allows the reconstruction of a volcanic island landscape and landform  
445 history in response to a contrasted climate. Exposed to the trade winds and associated relatively heavy  
446 rainfall, the northeast part of the island exhibits high denudation rates and deeply incised basins. The  
447 southern part of the island that currently receives low precipitation displays low denudation rates and  
448 gently southward dipping slopes. Accordingly, the denudation rates and the morphological evolution of  
449 the Santo Antão Island is probably primarily controlled by climatic processes. After comparison with  
450 previously published denudation rates from other islands, our data shows that the large climatic gradients  
451 existing on volcanic ocean islands have a predominant role on their landscape evolution. Our data  
452 represent additional inputs for construction of the global database of long-term denudation rates  
453 affecting volcanoes within tropical settings. The development of such database is key for better  
454 quantifying chemical and mechanical erosion processes in tropical environments.

455

## 456 **Acknowledgments**

457 The manuscript has been read by all authors, who have approved the content and agree to its publication.  
458 This study was supported by the INSU-CNRS SYSTER. We thank Emmanuel Davy for the  
459 mineralogical separation of the samples and Laurent Zimmerman for his assistance and help during He  
460 measurements.

## 461 **References**

462 Andrews, J. N., and R. L. F. Kay. 1982. Natural production of tritium in permeable rocks." *Nature* 298 (5872),  
463 361-363.

464 Balco, G., Stone, J.O., Lifton, N.A., and Dunai, T.J., 2008, A complete and easily accessible means of calculating  
465 surface exposure ages or erosion rates from  $^{10}\text{Be}$  and  $^{26}\text{Al}$  measurements: *Quaternary Geochronology* 3 (3), 174–  
466 195, doi:10.1016/j.quageo.2007.12.001.

467 Berner, R.A., Lasaga, A.C., and Garrels, R.M., 1983, The carbonate-silicate geochemical cycle and its effect on  
468 atmospheric carbon dioxide over the last 100 million years: *American Journal of Science* 283, 641–683, doi: 10  
469 .2475 /ajs .283 .7 .641

470 Blard, P.-H., Pik, R., Lavé, J., Bourlès, D., Burnard, P.G., Yokochi, R., Marty, B., Trusdell, F., 2006. Cosmogenic  
471 <sup>3</sup>He production rates revisited from evidences of grain size dependent release of matrix sited helium. *Earth Planet.*  
472 *Science Letter* 247, 222-234.

473 Blard, P. H., Lavé, J., Pik, R., Wagnon, P., Bourlès, D., 2007. Persistence of full glacial conditions in the central  
474 Pacific until 15,000 years ago. *Nature* 449 (7162), 591.

475 Blard, P. H., Farley, K. A., 2008. The influence of radiogenic <sup>4</sup>He on cosmogenic <sup>3</sup>He determinations in volcanic  
476 olivine and pyroxene. *Earth and Planetary Science Letters* 276 (1-2), 20-29.

477 Blard, P.-H., & Pik, R., 2008. An alternative isochron method for measuring cosmogenic <sup>3</sup>He in lava flows *Chem.*  
478 *Geol.* 251, 20-32

479 Blard, P.-H., Puchol, N., Farley, K.A., 2008. Constraints on the loss of matrix-sited helium during vacuum crushing  
480 of mafic phenocrysts. *Geochim. Cosmochim. Acta*, 72, 3788-3803.

481 Blard, P. H., Bourles, D., Pik, R., & Lavé, J., 2008. In situ cosmogenic <sup>10</sup>Be in olivines and pyroxenes.  
482 *Quaternary Geochronology* 3(3), 196-205.  
483

484 Charreau, J., Blard, P. H., Zumaque, J., Martin, L. C., Delobel, T., & Szafran, L., 2019. Basinga: A cell- by- cell  
485 GIS toolbox for computing basin average scaling factors, cosmogenic production rates and denudation rates. *Earth*  
486 *Surface Processes and Landforms* 44 (12), 2349-2365.

487 Dessert, C., Dupré, B., Gaillardet, J., François, L. M., & Allegre, C. J., 2003. Basalt weathering laws and the  
488 impact of basalt weathering on the global carbon cycle. *Chemical Geology* 202 (3-4), 257-273.

489 DiBiase, R. A., & Whipple, K. X., 2011. The influence of erosion thresholds and runoff variability on the  
490 relationships among topography, climate, and erosion rate. *Journal of Geophysical Research: Earth Surface*  
491 116(F4).

492 DiBiase, R. A., 2018. Increasing vertical attenuation length of cosmogenic nuclide production on steep slopes  
493 negates topographic shielding corrections for catchment erosion rates. *Earth Surface Dynamics* 6(4).

494 Dunai, T., 2000. Scaling factors for production rates of in situ produced cosmogenic nuclides: A critical  
495 reevaluation: *Earth and Planetary Science Letters* 176 (1), 157–169, doi:10.1016/S0012-821X(99)00310-6.

496 Duncan, R. A. & Jackson, E. D., 1977. Geochronology of basaltic rocks recovered by DSDP Leg 41, Eastern  
497 Atlantic Ocean. In: Lancelot, Y., Seibold, E., et al. (eds) *Initial Report of the Deep Sea Drilling Project*, 41,  
498 Washington, DC: US Government Printing Office, 1113–1118.

499 Ferrier, K. L., Perron, J. T., Mukhopadhyay, S., Rosener, M., Stock, J. D., Huppert, K. L., & Slosberg, M., 2013.  
500 Covariation of climate and long-term erosion rates across a steep rainfall gradient on the Hawaiian island of Kaua  
501 i. *Bulletin* 125 (7-8), 1146-1163.

502 Foeken, J. P., Stuart, F. M., & Mark, D. F., 2012. Long-term low latitude cosmogenic <sup>3</sup>He production rate  
503 determined from a 126 ka basalt from Fogo, Cape Verdes. *Earth and Planetary Science Letters* 359, 14-25.

504 Gaillardet J., Dupre B., Louvat P., Allegre C.J., 1999. Global silicate weathering and CO<sub>2</sub> consumption rates  
505 deduced from the chemistry of large rivers. *Chemical Geology*, 159 (1-4), 3-30

506 Gayer E., Mukhopadhyay S., Meade B.J., 2008. Spatial variability of erosion rates inferred from the frequency  
507 distribution of cosmogenic <sup>3</sup>He in olivines from Hawaiian river sediments. *Earth Planet. Sci. Lett.* 266, 303-315.

508 Granger, D. E., Kirchner, J. W., & Finkel, R., 1996. Spatially averaged long-term erosion rates measured from in  
509 situ-produced cosmogenic nuclides in alluvial sediment. *The Journal of Geology* 104 (3), 249-257.

510 Hayes, D. E., & Rabinowitz, P. D., 1975. Mesozoic magnetic lineations and the magnetic quiet zone off northwest  
511 Africa. *Earth and Planetary Science Letters* 28 (2), 105-115.

512 Hildenbrand, A., Gillot, P.Y., Marlin, C., 2008. Geomorphological study of long-term erosion on a tropical  
513 volcanic ocean island: Tahiti-Nui (French Polynesia), *Geomorphology* 93 (3-4), 460-481,  
514 doi:10.1016/j.geomorph.2007.03.012.

515 Hooghiemstra, H., 1989. Variations of the NW African trade wind regime during the last 140 000 years: changes  
516 in pollen flux evidenced by marine sediment records. In *Paleoclimatology and paleometeorology: modern and past*  
517 *patterns of global atmospheric transport*. Springer, Dordrecht. 733-770.

518 Holm, P. M., Wilson, J. R., Christensen, B. P., Hansen, L., Hansen, S. L., Hein, K. M., Mortensen, A. K., Pederson,  
519 R., Plesner, S., Runge, M. K., 2005. Sampling the Cape Verde mantle plume: evolution of melt compositions on  
520 Santo Antão, Cape Verde Islands. *Journal of Petrology* 47 (1), 145-189.

521 Jefferson, A. J., Ferrier, K. L., Perron, J. T., Ramalho, R., 2014. Controls on the hydrological and topographic  
522 evolution of shield volcanoes and volcanic ocean islands. *The Galapagos: A natural laboratory for the Earth*  
523 *Sciences* 204, 185-213.

524 Jolliffe, I.T., 2002. *Principal Component Analysis*, Series: Springer Series in Statistics, 2nd ed., Springer, NY,  
525 XXIX, 487 p. 28 illus. ISBN 978-0-387-95442-4.

526 Kirchner, J. W., Riebe, C. S., Ferrier, K. L., Finkel, R. C., 2006. Cosmogenic nuclide methods for measuring long-  
527 term rates of physical erosion and chemical weathering. *Journal of Geochemical Exploration* 88 (1-3), 296-299.

528 Kurz, M.D., 1986. Cosmogenic helium in a terrestrial igneous rock: *Nature* 320, 435-439, doi:10.1038/320435a0.

529 Lahitte, P., Samper, A., Quidelleur, X., 2012. DEM-based reconstruction of southern Basse-Terre volcanoes  
530 (Guadeloupe archipelago, FWI): Contribution to the Lesser Antilles Arc construction rates and magma production.  
531 *Geomorphology* 136 (1), 148-164.

- 532 Lal, D., 1991. Cosmic ray labeling of erosion surfaces: in situ nuclide production rates and erosion models. *Earth*  
533 *and Planetary Science Letters* 104 (2-4), 424-439.
- 534 Langbein, W. B., & Schumm, S. A., 1958. Yield of sediment in relation to mean annual precipitation. *Eos,*  
535 *Transactions American Geophysical Union* 39 (6), 1076-1084.
- 536 Lenton, T.M., Britton, C., 2006. Enhanced carbonate and silicate weathering accelerates recovery from fossil fuel  
537 CO<sub>2</sub> perturbations. *Global Biogeochemical Cycles* 20 (3), GB3009.
- 538 List, F. K., Klitzsch, E., Kusserow, H., Munier, K., Munier, C., Levenhagen, J., 2007. Cape Verde Islands: Santo  
539 Antão, São Vicente, Sal, Fogo, Thematic Maps, Geology. Amt Für Geoinformationsweser der Bundeswehr  
540 (AGeoBW)/Geoinformation Office of the German Armed Forces.
- 541 Louvat, P., & Allègre, C. J., 1997. Present denudation rates on the island of Reunion determined by river  
542 geochemistry: basalt weathering and mass budget between chemical and mechanical erosions. *Geochimica et*  
543 *Cosmochimica Acta* 61 (17), 3645-3669.
- 544 Mannaerts, C. M., & Gabriels, D., 2000. Rainfall erosivity in Cape Verde. *Soil and Tillage Research* 55 (3-4), 207-  
545 212.
- 546 Matsuda, J., Matsumoto, T., Sumino, H., Nagao, K., Yamamoto, J., Miura, Y., Kaneoka, I., Takahata, N., Sano,  
547 Y., 2002. The <sup>3</sup>He/<sup>4</sup>He ratio of the new internal He Standard of Japan (HESJ). *Geochemical Journal* 36 (2), 191-  
548 195.
- 549 Menéndez, I., Silva, P. G., Martín-Betancor, M., Pérez-Torrado, F. J., Guillou, H., Scaillet, S., 2008. Fluvial  
550 dissection, isostatic uplift, and geomorphological evolution of volcanic islands (Gran Canaria, Canary Islands,  
551 Spain). *Geomorphology* 102 (1), 189-203.
- 552 Mitchell, J. G., Le Bas, M. J., Zielonka, J., Furnes, H., 1983. On dating the magmatism of Maio, Cape Verde  
553 islands. *Earth and Planetary Science Letters* 64 (1), 61-76.
- 554 Plesner, S., Holm, P. M., Wilson, J. R., 2002. <sup>40</sup>Ar/<sup>39</sup>Ar geochronology of Santo Antao, Cape Verde Islands.  
555 *Journal of Volcanology and Geothermal Research* 120, 103–121.
- 556 Portenga, E. W., & Bierman, P. R., 2011. Understanding Earth's eroding surface with <sup>10</sup>Be. *GSA today* 21 (8),  
557 4-10.
- 558 Protin, M., Blard, P. H., Marrocchi, Y., Mathon, F., 2016. Irreversible adsorption of atmospheric helium on olivine:  
559 A lobster pot analogy. *Geochimica et Cosmochimica Acta* 179, 76-88.
- 560 Puchol, N., Blard, P. H., Pik, R., Tibari, B., Lavé, J., 2017. Variability of magmatic and cosmogenic <sup>3</sup>He in  
561 Ethiopian river sands of detrital pyroxenes: Impact on denudation rate determinations. *Chemical Geology* 448, 13-  
562 25.
- 563 Rognon, P., Coudé-Gaussens, G., Revel, M., Grousset, F. E., Pedemay, P., 1996. Holocene Saharan dust deposition  
564 on the Cape Verde Islands: sedimentological and Nd-Sr isotopic evidence. *Sedimentology* 43 (2), 359-366.

565 Ricci, J., Lahitte, P., Quidelleur, X., 2015. Construction and destruction rates of volcanoes within tropical  
566 environment: Examples from the Basse-Terre Island (Guadeloupe, Lesser Antilles). *Geomorphology* 228, 597-  
567 607.

568 Salvany, T., Lahitte, P., Nativel, P., Gillot, P. Y., 2012. Geomorphic evolution of the Piton des Neiges volcano  
569 (Réunion Island, Indian Ocean): competition between volcanic construction and erosion since 1.4 Ma.  
570 *Geomorphology* 136 (1), 132-147.

571 Sarda, P., Staudacher, T., Allègre, C. J., Lecomte, A., 1993. Cosmogenic neon and helium at Réunion:  
572 measurement of erosion rate. *Earth and Planetary Science Letters* 119 (3), 405-417.

573 Willett, S. D., 1999. Orogeny and orography: The effects of erosion on the structure of mountain belts. *Journal of*  
574 *Geophysical Research: Solid Earth* 104 (B12), 28957-28981.

575 Whipple, K.X., 2009, The influence of climate on the tectonic evolution of mountain belts. *Nature Geoscience* 2,  
576 97-104, doi: 10.1038/ngeo413.

577 Zimmermann, L., Blard, P. H., Burnard, P., Medynski, S., Pik, R., Puchol, N., 2012. A new single vacuum furnace  
578 design for cosmogenic  $^3\text{He}$  dating. *Geostandards and Geoanalytical Research* 36 (2), 121-129.

579

580

## 581 **Figure captions**

582 Figure 1. Overview of the Cape Verde islands and ASTER satellite images of Santo Antão Island.

583

584 Figure 2. Simplified geological map of Santo Antão modified from List et al. (2007).

585

586 Fig 3. a. Precipitation and elevation maps over Santo Antão Island from TRMM. The black arrows show  
587 the main direction of the wind. b. Photograph of the dry region of Tarrafal on the southwest side of the  
588 island. c. Photograph of the wetter valley of the Ribeira on the northeast side of the island.

589

590

591 Fig 4: a.  $^3\text{He}_c$  calculated with the first approach (Eq. 4) versus the  $^3\text{He}_c$  calculated with the second  
592 approach (Eq. 5). b. Denudation rates calculation from the first approach versus the denudation rates  
593 calculation from the second approach. The grey band represents the single prediction band of the one  
594 standard deviation of the correlation trend in red.

595

596

597 Figure 5: Comparison of the replicate measures of the denudation rates. a. Comparison of the replicates  
598 of the denudation rates calculated with the first approach. b. Comparison of the replicates of the  
599 denudation rates calculated with the second approach. c. Comparison of the replicates of the denudation  
600 rates calculated with the two approaches together. D. Zoom of the Fig. 5c showing the best  
601 reproducibility of the measurements for denudation rates lower than ~15 m/Ma.  
602

603 Figure 6: Spatial variation of the denudation rates on Santo Antão Island.

604

605 Figure 7: Map of the slope distribution on Santo Antão and hillshade map on the left top side. The north  
606 and northeast side of the island as well show high slopes corresponding to the dissected valleys. The  
607 edges of the Cha di Morte also show high slope angles, whereas the south of the island shows relatively  
608 low slope angles corresponding to a smooth morphology.

609

610 Figure 8: Log-ratio transformed compositional biplots derived from principle component analysis. The  
611 length of the black rays is proportional to the amount of variation explained by the corresponding  
612 controlling factors. Samples taken from different basins are clustered according to their calculated  
613 denudation rates with the second approach.

614

615

616 Figure 9: Denudation rates measured on different volcanic islands in the world using logarithmic scales.  
617 The square symbols correspond to computed denudation rates based on eroded volume, whereas the  
618 triangles correspond to denudation rates based on  $^3\text{He}$  cosmogenic concentration.

619

620

Table 1

Sample name	Phenocryst	Fraction	Aliquot mass	<sup>3</sup> He(melt)	<sup>4</sup> He(melt)	1st approach					2nd approach		Integration time	
						P <sub>4</sub> (radiogenic)	<sup>4</sup> He (radiogenic)	P <sub>3</sub> (nucleogenic)	<sup>3</sup> He (nucleogenic)	<sup>3</sup> He (cosmogenic)	Denudation rate	<sup>3</sup> He (cosmogenic)		Denudation rate
		(μm)	(g)	(10 <sup>6</sup> at/g)	(10 <sup>12</sup> at/g)	(10 <sup>6</sup> at/g/yr)	(10 <sup>12</sup> at/g)	(10 <sup>-2</sup> at/g/yr)	(10 <sup>4</sup> at/g)	(10 <sup>6</sup> at/g)	(m/Ma)	(10 <sup>6</sup> at/g)	(m/Ma)	(ka)
						with U, Th and Sm in lava = 0								
CV18-01	Px	140-500	0.2331	21.7 ± 1.00	1.67 ± 0.05	1.73	1.17 ± 0.39	1.57	1.65 ± 0.55	13.3 ± 1.29	4.67 ± 0.46	19.0 ± 1.02	3.30 ± 0.2	164
CV18-01	Px	140-500	0.1765	25.3 ± 0.06	1.95 ± 0.04	1.73	1.17 ± 0.39	1.57	1.65 ± 0.55	12.1 ± 0.85	5.11 ± 0.39	22.6 ± 0.63	2.70 ± 0.09	195
CV18-02	Px	140-500	0.2569	17.7 ± 0.08	5.22 ± 0.14	2.75	2.18 ± 0.22	0.08	0.08 ± 0.01			13.0 ± 0.88	7.40 ± 0.66	72
CV18-03	Px	140-500	0.2404	17.7 ± 0.08	1.46 ± 0.04	2.25	1.49 ± 0.49	2.74	2.88 ± 0.96	17.7 ± 1.16	4.50 ± 0.31	15.4 ± 0.85	5.20 ± 0.30	103
CV18-03	Px	140-500	0.3403	16.6 ± 0.07	1.21 ± 0.04	2.25	1.49 ± 0.49	2.74	2.88 ± 0.96	16.5 ± 1.10	4.81 ± 0.33	14.3 ± 0.77	5.60 ± 0.32	96
CV18-04	Px	140-500	0.2558	29.0 ± 1.28	2.00 ± 0.06	1.38	0.75 ± 0.25	1.21	1.27 ± 0.42	7.91 ± 1.61	12.7 ± 2.61	18.2 ± 1.37	5.50 ± 0.43	96
CV18-04	Px	140-500	0.1998	30.8 ± 1.36	2.18 ± 0.07	1.38	0.75 ± 0.25	1.21	1.27 ± 0.42	6.68 ± 1.82	15.1 ± 4.12	19.9 ± 1.46	5.00 ± 0.38	106
CV18-05	Px	140-500	0.2374	9.48 ± 0.53	1.28 ± 0.04	2.15	2.91 ± 1.78	1.28	2.30 ± 1.41	9.42 ± 1.36	10.2 ± 1.47	6.34 ± 0.56	15.2 ± 1.38	35
CV18-05	Px	140-500	0.2869	11.0 ± 0.54	1.41 ± 0.04	2.15	2.91 ± 1.78	1.28	2.30 ± 1.41	10.9 ± 1.39	8.80 ± 1.13	7.84 ± 0.58	12.3 ± 0.95	43
CV18-06	Px	75-500	0.2594	8.99 ± 0.49	1.26 ± 0.04	1.55	2.30 ± 2.04	0.80	1.81 ± 1.60	8.98 ± 1.22	9.06 ± 1.24	3.38 ± 0.57	24.0 ± 4.06	22
CV18-06	Px	75-500	0.2546	13.6 ± 0.34	2.39 ± 0.05	1.55	2.30 ± 2.04	0.80	1.81 ± 1.60	12.0 ± 0.96	6.77 ± 0.56	7.94 ± 0.44	10.2 ± 0.61	52
CV18-07	Px	75-500	0.2846	15.7 ± 0.72	1.26 ± 0.04	1.15	2.83 ± 1.64	1.17	5.55 ± 3.22	15.5 ± 1.98	6.41 ± 0.83	9.49 ± 0.79	10.4 ± 0.90	51
CV18-07	Px	75-500	0.2764	20.2 ± 0.45	1.54 ± 0.03	1.15	2.83 ± 1.64	1.17	5.55 ± 3.22	20.2 ± 1.76	4.91 ± 0.44	14.2 ± 0.56	7.00 ± 0.31	77
CV18-08	Px	140-500	0.2884	8.90 ± 0.48	2.01 ± 0.06	2.41	6.10 ± 5.34	1.79	7.17 ± 6.28	8.83 ± 3.34	10.4 ± 3.94	3.87 ± 0.58	23.7 ± 3.58	23
CV18-08	Px	140-500	0.2852	9.18 ± 0.26	1.93 ± 0.04	2.41	6.10 ± 5.34	1.79	7.17 ± 6.28	9.11 ± 3.27	10.1 ± 3.62	4.16 ± 0.41	22.1 ± 2.21	24
CV18-09	Px	140-500	0.2846	3.78 ± 0.29	1.40 ± 0.04	1.90	1.17 ± 0.39	1.29	1.36 ± 0.45			2.76 ± 0.36	33.3 ± 4.41	16
CV18-10	Px	140-500	0.3100	6.25 ± 0.37	1.45 ± 0.04	2.43	3.32 ± 3.07	1.88	4.06 ± 3.76	6.21 ± 1.76	14.8 ± 4.23	4.99 ± 0.44	18.4 ± 1.69	29
CV18-11	Px	140-500	0.2705	2.91 ± 0.27	1.46 ± 0.04	2.44	4.55 ± 3.37	1.21	3.28 ± 2.43	2.88 ± 2.26	31.9 ± 25.11	2.03 ± 0.29	45.2 ± 6.65	12
CV18-11	Px	140-500	0.3562	5.48 ± 0.16	2.55 ± 0.05	2.44	4.55 ± 3.37	1.21	3.28 ± 2.43	5.45 ± 1.87	16.9 ± 5.81	4.61 ± 0.21	20.0 ± 0.98	27
CV18-12	Px/oliv	140-500	0.2466	3.01 ± 0.31	1.51 ± 0.04	2.48	4.18 ± 3.64	1.20	2.77 ± 2.41	2.98 ± 1.92	32.1 ± 20.1	2.96 ± 0.33	32.2 ± 3.68	17
CV18-12	Px/oliv	140-500	0.2837	2.61 ± 0.19	2.08 ± 0.04	2.48	4.18 ± 3.64	1.20	2.77 ± 2.41	2.58 ± 1.66	37.1 ± 23.8	2.56 ± 0.17	37.4 ± 2.57	14
CV18-13	Px	140-500	0.2459	4.09 ± 0.34	1.33 ± 0.04	1.56	3.37 ± 1.95	1.61	7.63 ± 4.42	4.01 ± 2.64	19.1 ± 12.6	3.59 ± 0.37	21.4 ± 2.24	25
CV18-14	Px	140-500	0.2991	4.23 ± 0.29	0.94 ± 0.03	4.36	8.37 ± 7.28	1.42	3.26 ± 2.84	4.20 ± 3.82	16.6 ± 15.1	3.29 ± 0.37	21.3 ± 2.45	25
CV18-17	Px	140-500	0.3099	4.44 ± 0.29	5.60 ± 0.15	12.5	33.6 ± 29.0	2.86	8.29 ± 7.14	4.36 ± 13.0	21.1 ± 62.8	3.11 ± 0.34	29.5 ± 3.25	18
CV18-18	Px	140-500	0.1818	10.8 ± 0.63	2.70 ± 0.08	4.06	4.58 ± 3.16	1.58	2.29 ± 1.58	10.8 ± 1.96	6.11 ± 1.11	10.1 ± 0.64	6.51 ± 0.44	82
CV18-19	Px/oliv	140-500	0.3134	2.88 ± 0.25	1.57 ± 0.04	0.91	1.08 ± 0.47	0.42	0.87 ± 0.38			2.63 ± 0.28	39.9 ± 4.35	13
CV18-20	Px/oliv	140-500	0.3135	2.53 ± 0.24	3.49 ± 0.09	1.01	1.21 ± 0.53	0.41	0.85 ± 0.37			1.94 ± 0.29	57.5 ± 3.84	9
CV18-25	Px	140-500	0.2216	2.20 ± 0.30	1.12 ± 0.03	0.93	1.57 ± 1.04	1.09	4.92 ± 3.28	2.15 ± 1.43	47.2 ± 31.4	2.08 ± 0.35	47.8 ± 8.16	11
CV18-26	Px/oliv	140-500	0.2916	4.20 ± 0.30	1.42 ± 0.04	1.21	1.47 ± 1.47	0.64	1.29 ± 1.29	4.18 ± 0.85	26.1 ± 5.35	2.98 ± 0.35	36.6 ± 4.37	15
CV18-27	Px/oliv	140-500	0.2925	13.1 ± 0.58	0.13 ± 0.01	13.1	1.25 ± 0.03	3.45	0.36 ± 0.01	13.1 ± 0.80	9.34 ± 0.60	12.6 ± 0.62	9.65 ± 0.51	55
CV18-28	Px/oliv	140-500	0.3783	14.6 ± 0.66	4.80 ± 0.13	4.36	0.93 ± 0.31	2.25	0.67 ± 0.22			12.9 ± 0.68	5.33 ± 0.27	100
CV18-29	Px	140-500	0.2037	13.4 ± 0.68	0.60 ± 0.02	1.26	0.67 ± 0.27	0.74	0.73 ± 0.29	13.3 ± 0.84	6.31 ± 0.42	13.0 ± 0.71	6.46 ± 0.37	83

Figure 1 (Color)

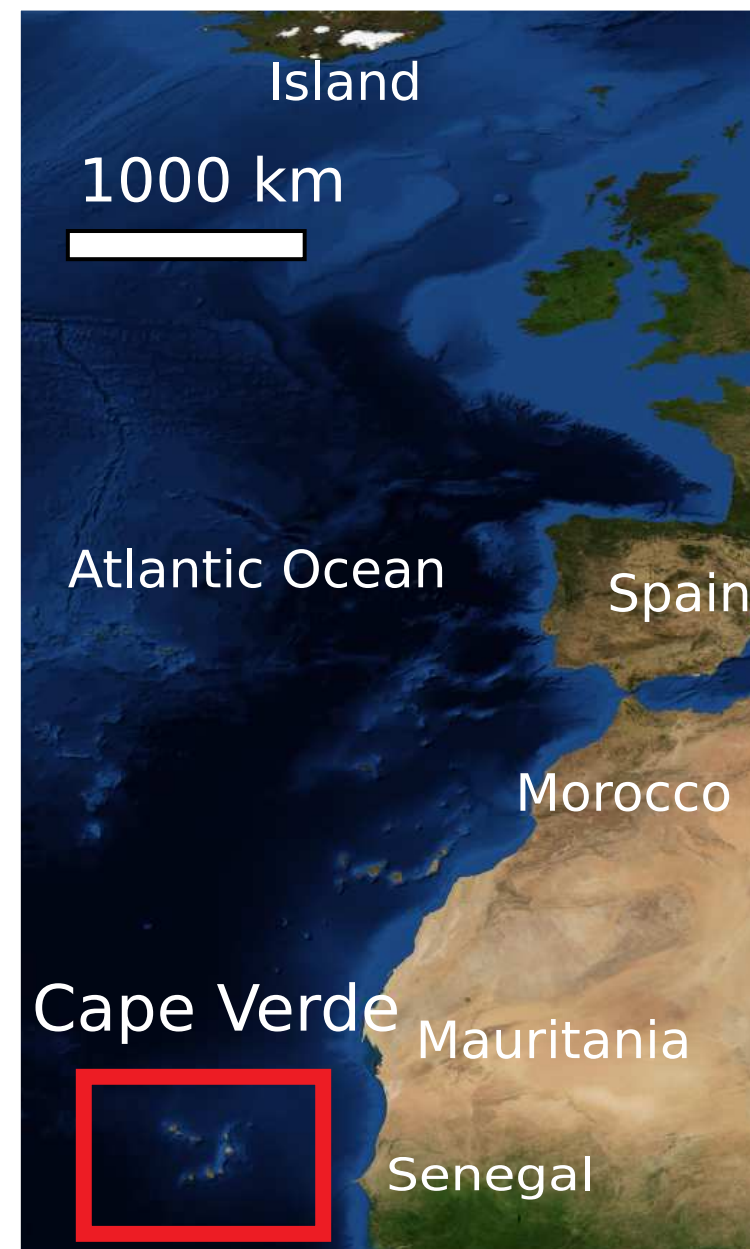


Figure 2 (Color)

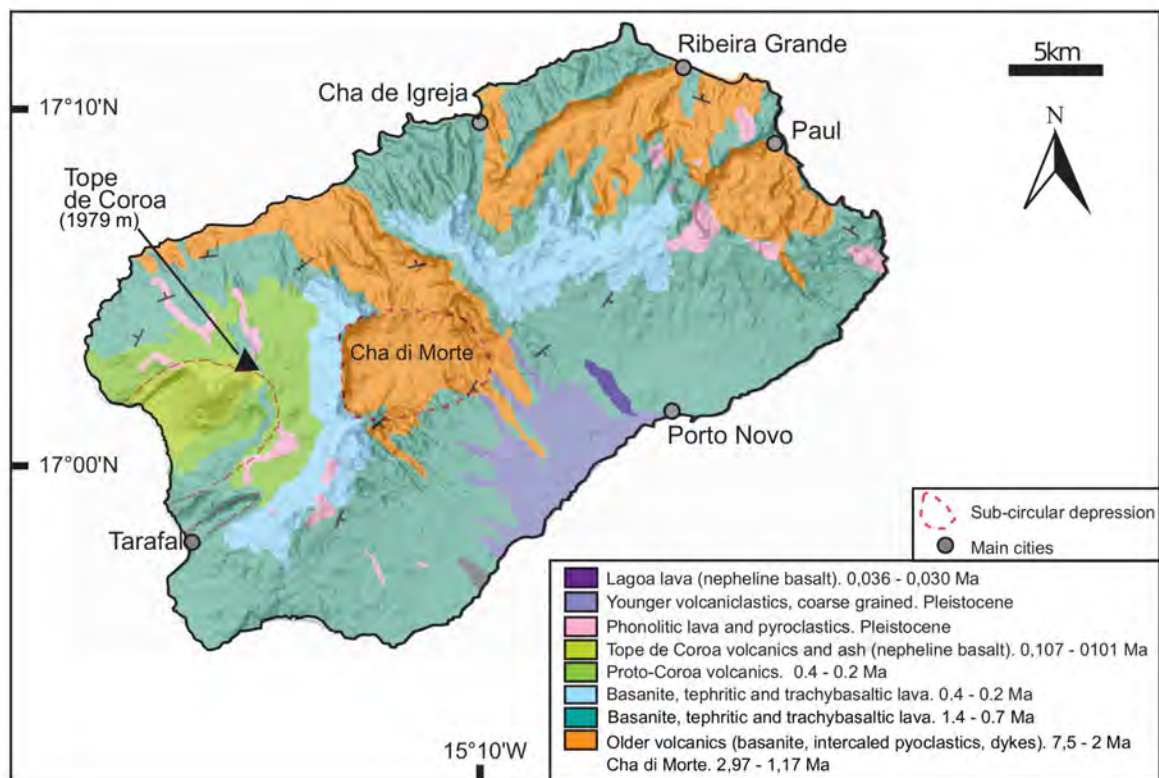


Figure 3 (Color)

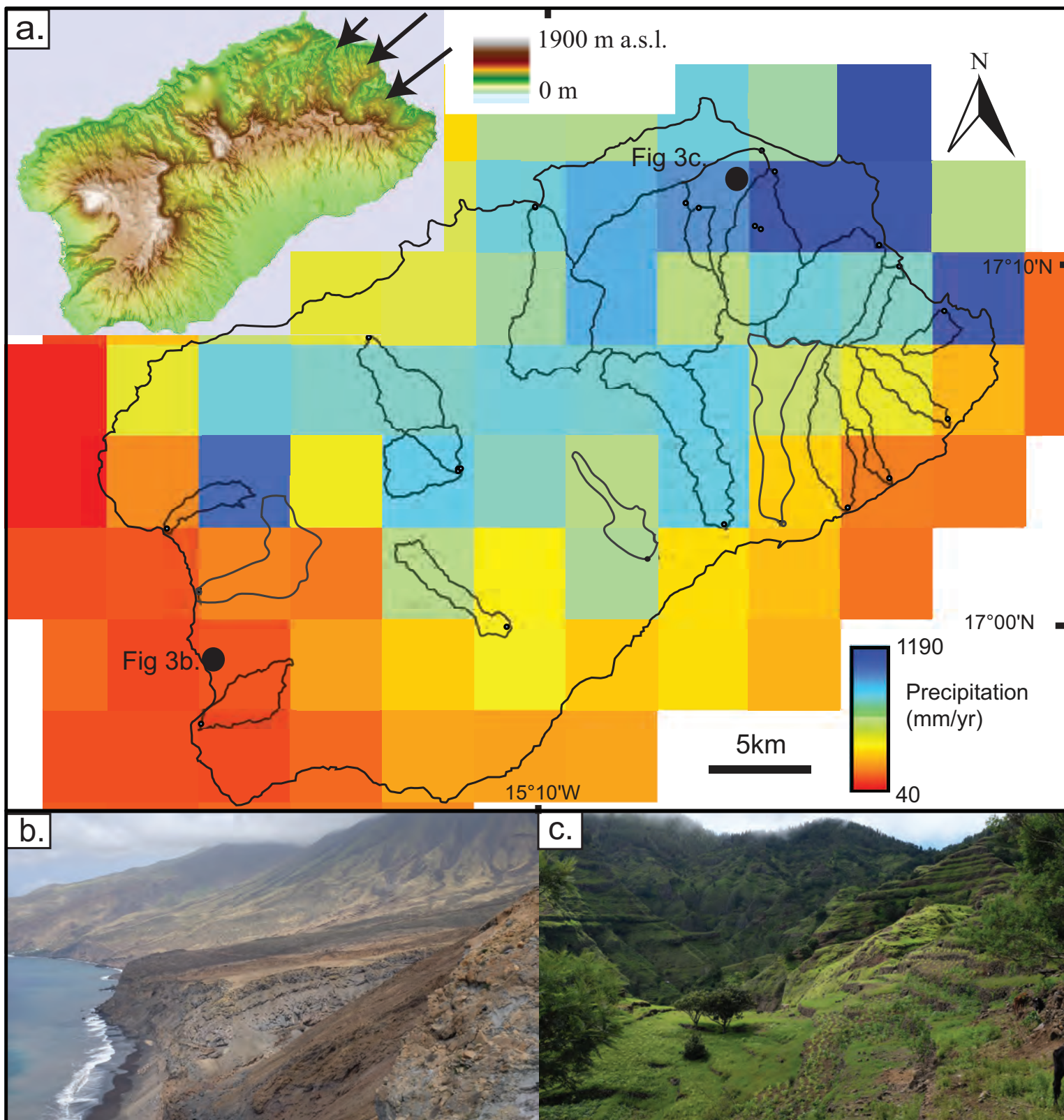


Figure 4 (Color)

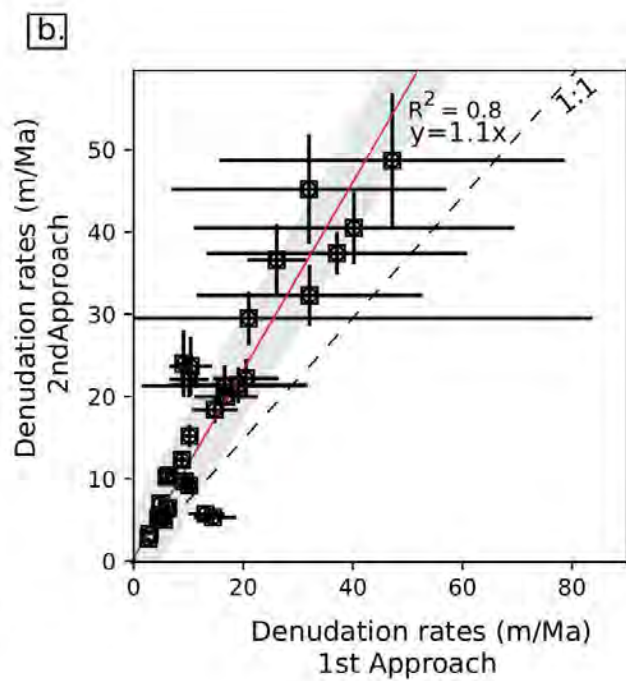
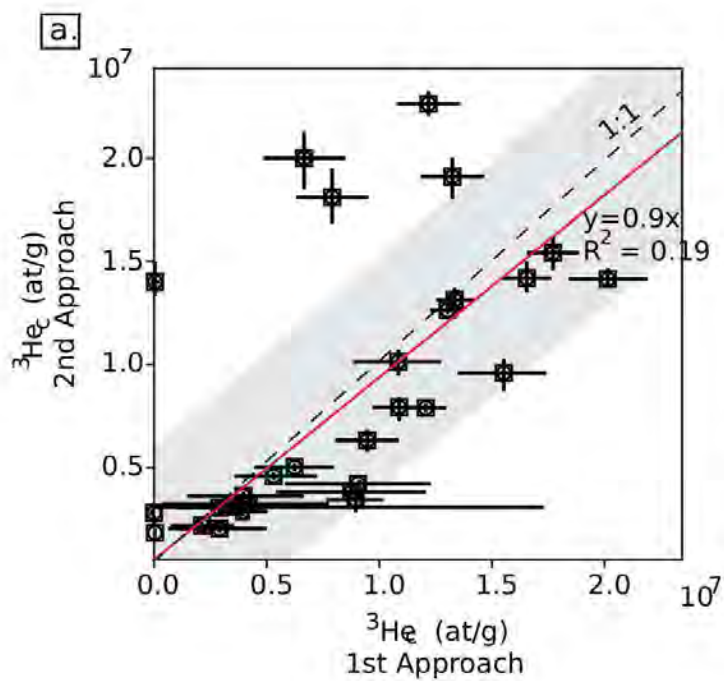
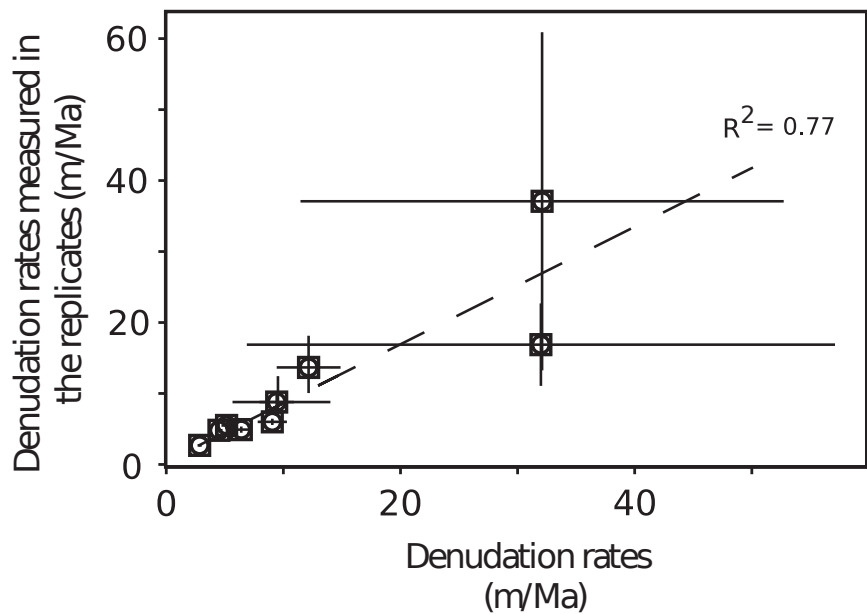
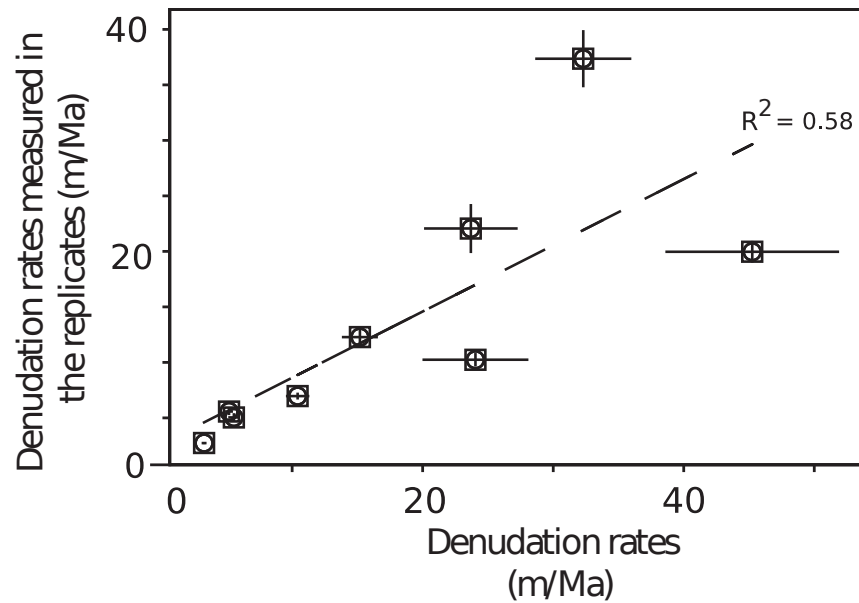


Figure 5 (Color)

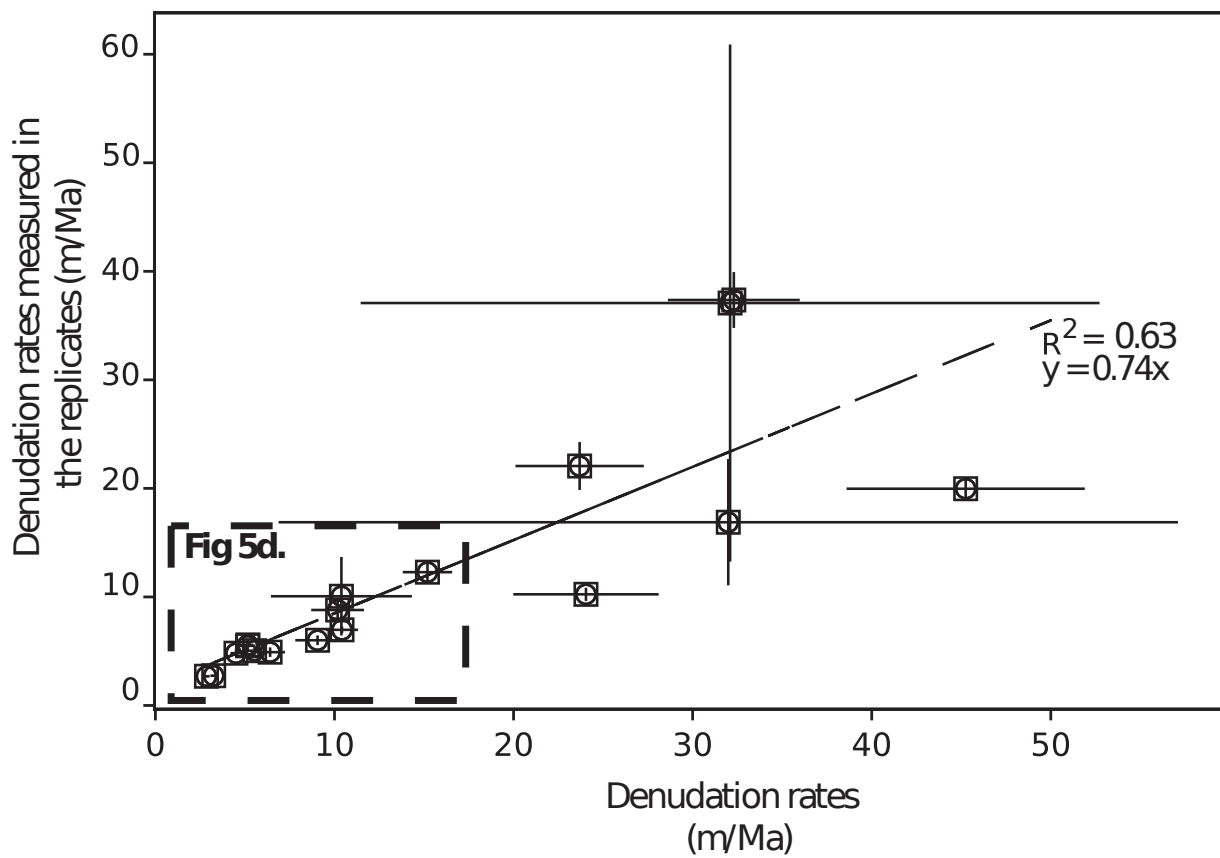
**a. 1st Approach**



**b. 2nd Approach**



**c. The 2 approaches combined**



**d. zoom of Fig 5c.**

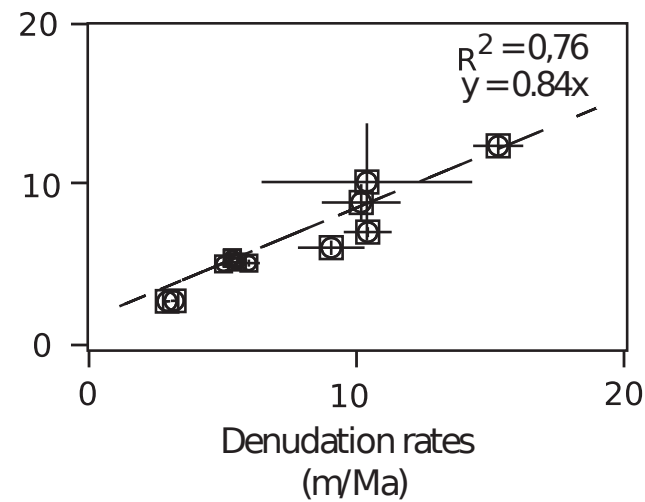


Figure 6 (Color)

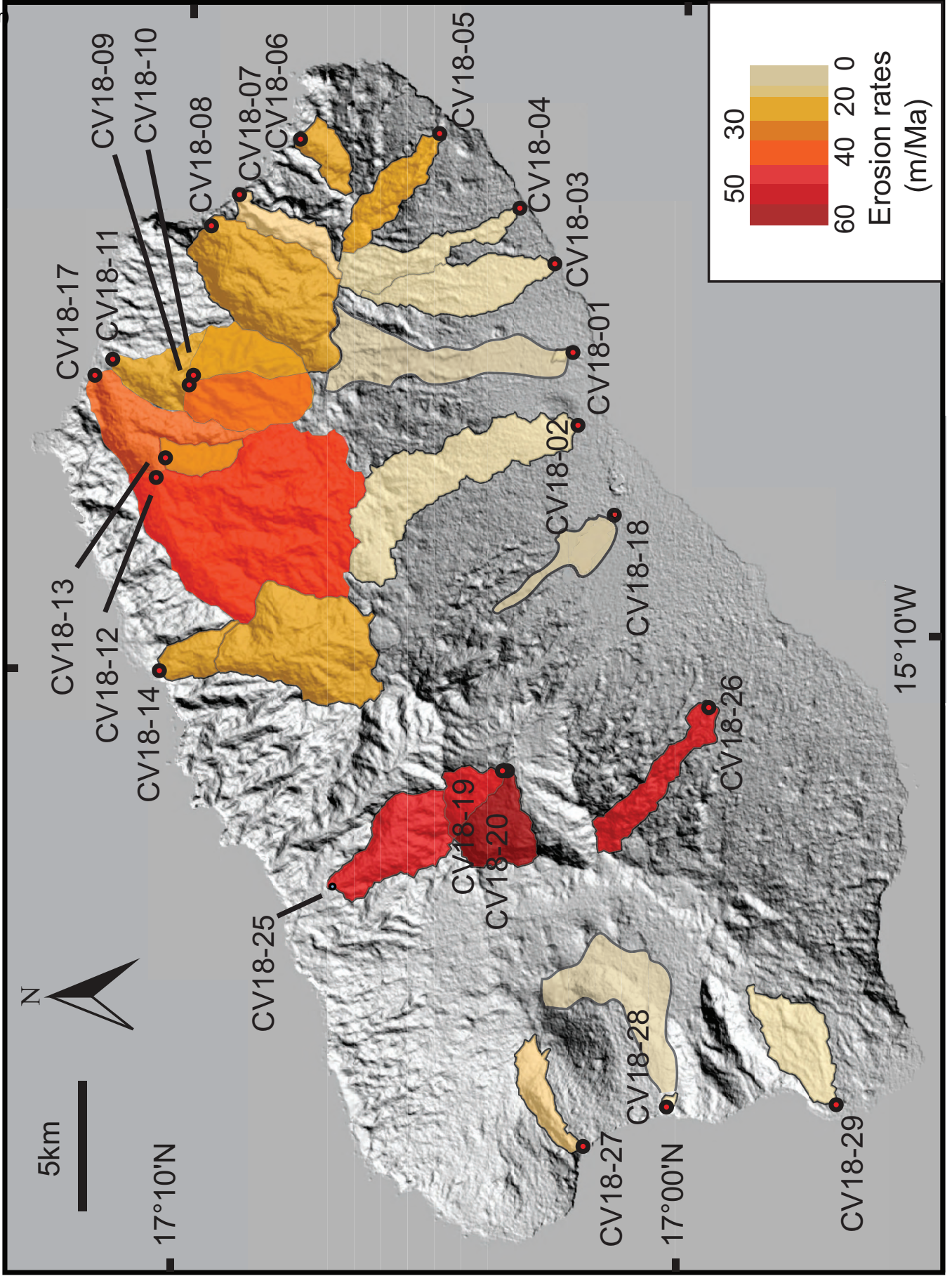


Figure 7 (Color)

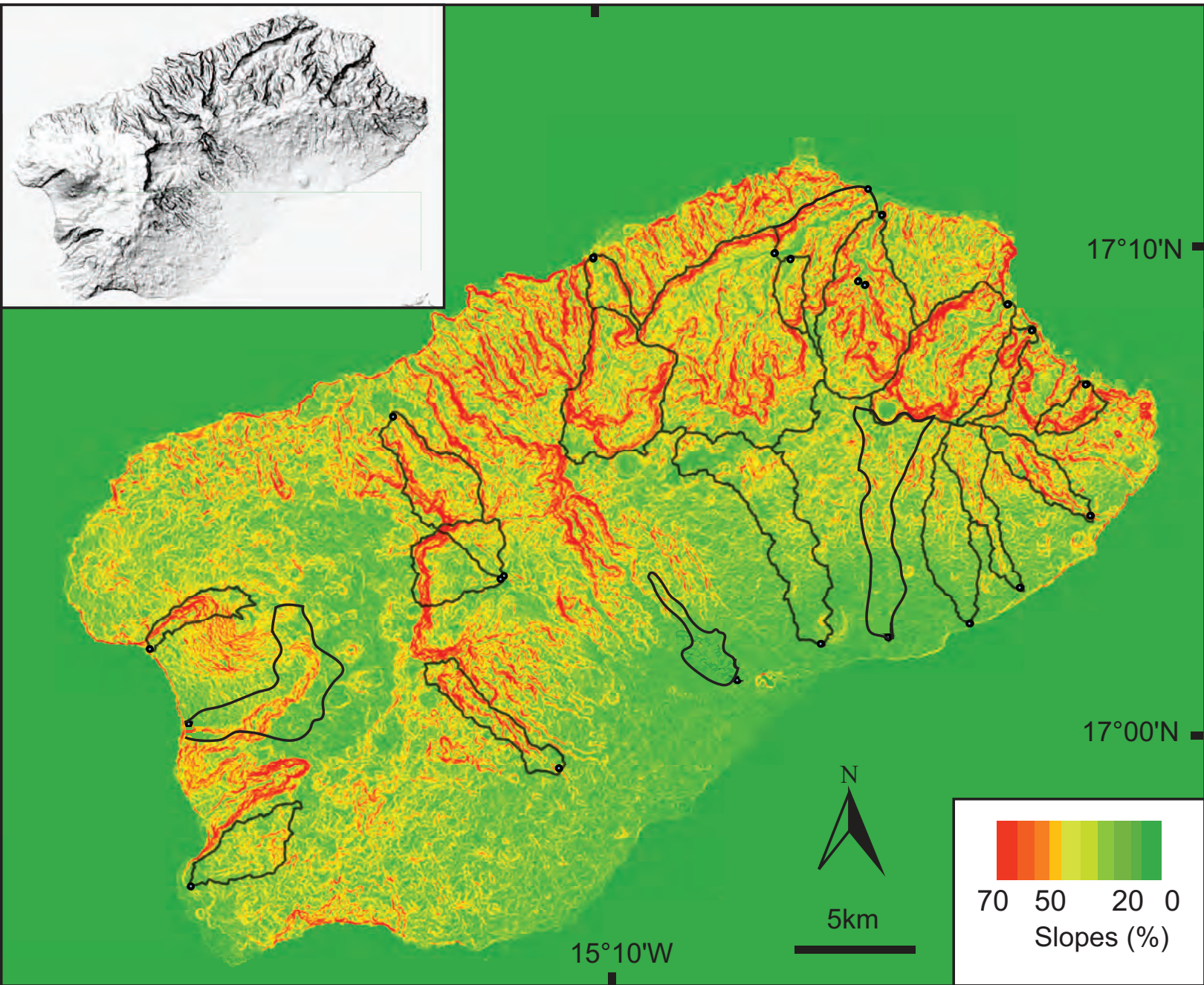


Figure 8 (Color)

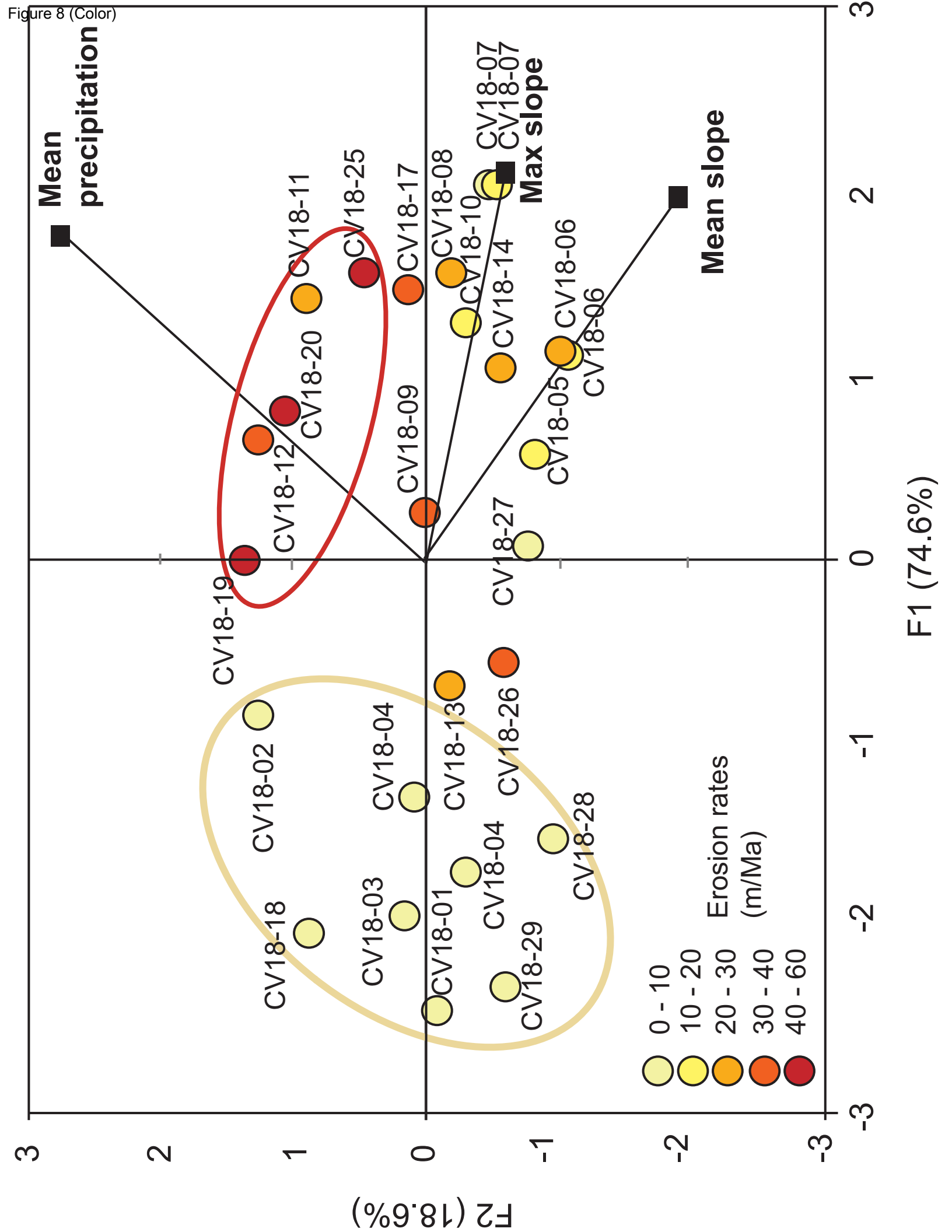
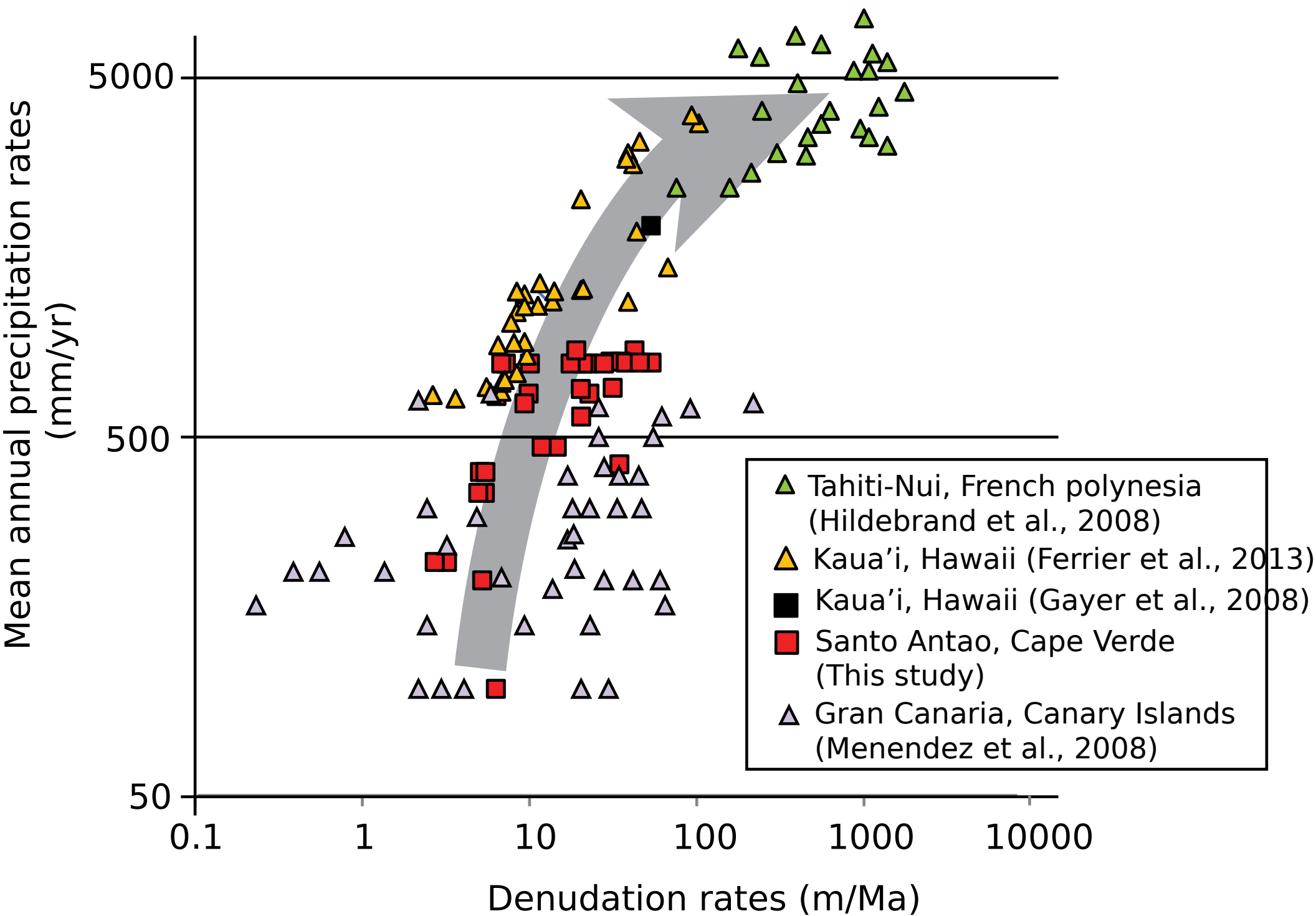
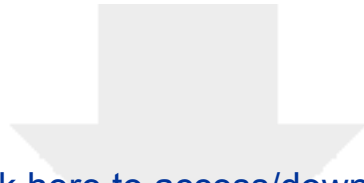


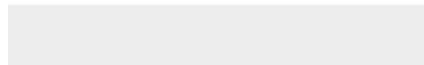
Figure 9 (Color)





[Click here to access/download](#)

**Supplementary material for online publication only**  
**TableA1.xlsx**





[Click here to access/download](#)

**Supplementary material for online publication only**  
**TableA2.xlsx**





[Click here to access/download](#)

**Supplementary material for online publication only**  
**TableA3.xlsx**

